# Evaluating the Effects of Scan Strategy on AM Annealed Fe-3Si steel through Understanding of Solidification Conditions and Thermal Stresses

A Thesis Presented for the
Master of Science
Degree
The University of Tennessee, Knoxville

Michael P. Haines
August 2020

# DEDICATION

This thesis is dedicated to my mother and father, Sue and Dave Haines and my brother David, who supported me through my graduate studies and research.

# ACKNOWLEDGEMENTS

I would like to thank Prof. Suresh Babu and Dr. Alex Plotkowski, my advisors who supported me during my research. I would also like to thank the people at ORNL for their support of my research and for allowing me access to their facilities. I would like to specifically thank Fred List III, Keith Carver, Andrés Rossy and the people who work at the Zeiss material characterization lab at the MDF for their contributions to my research. Lastly, I would like to thank Suresh's student group for their support and friendship: Sabina, Cullen, Kevin, Kevin, Kevin, Michael, Eric, Sujana, Amy, Caitlin, Serena, Vanshika, Stephen, Alex, Sean, and Obed.

# ABSTRACT

Soft magnetic steels have seen recent adoption in additive manufacturing (AM) due to the prospect of reducing eddy currents and hysteresis losses through leveraging of complex geometries and microstructural control. An annealing step will be a significant step for these alloys produced in AM to increase grain size and further reduce hysteresis losses. In this study, thin wall Fe-3Si samples were produced using laser powder bed fusion (L-PBF) using two different scan strategies, with a subset of samples annealed at 1200°[degrees]C for 5 minutes. The effects of the two different scan strategies on microstructure in the as-built and annealed samples were analyzed through Electron Back Scatter Diffraction (EBSD) where it was found that the scan strategy does have an effected on annealed microstructure. Thermal simulations using OpenFOAM were used to rationalize the differences in microstructure formation between the two scan strategies for the as-built scan strategies by looking at the thermal gradients and solidification velocity, while explanations on why there is a difference in resulting annealed microstructure was made by looking at the grain orientation, size and misorientation. Further, thermal-mechanical simulations were conducted using Abaqus to see if differences in the resulting elastic and plastic strains due to differences in thermal stresses related to the two difference scan strategies could be a mechanism causing differences in annealed microstructure to occur.

# TABLE OF CONTENTS

# LIST OF TABLES

# LIST OF FIGURES

# CHAPTER 1: INTRODUCTION

Additive manufacturing (AM) is an appealing technology for its ability to produce complex geometries for a wide range of structural applications. While conventional manufacturing techniques traditionally rely on subtractive methods such as milling and turning, AM relies on material being added layer-by-layer to construct a near-net shape part and has the added benefit of being able to create more complex geometries while having a lower buy-to-fly ratio [1] . Laser Powder Bed Fusion (L-PBF), the method used in this thesis, relies on a laser to melt layers of powder. The repeated melting of powdered layered result in the final build geometry. Due to the complexity of the processes a large amount of research in recent years has gone into studying the resulting microstructural and mechanical properties of materials used in L-PBF [2].

Compared to wrought and cast alloy parts, L-PBF produced parts see much higher cooling rates (between $10^3$ – $10^6$ $Ks^{-1}$) [3–6], and therefore have unique material characteristics, and mechanical properties compared to other traditional production techniques. Thus, studies need to be carried out on resulting microstructure when the material is produced under L-PBF. A case example would be IN718 which under traditional wrought and casting conditions would see the formation of the $\gamma''$ phase, however due to the quick solidification rates in L-PBF, IN718 produced under L-PBF sees no $\gamma''$ phase formation [7]. Likewise, a study on Al-Ce alloys showed that due to the very high cooling rates seen in L-PBF finer microstructures with non-equilibrium solidification conditions such that variations in elemental segregation were noted to occur [8].

Further, due to the complex control over laser scanning patterns, additive manufacturing offers the opportunity for fine control over the cooling rates thus allowing for unique control over microstructure formation. While this fine control is most evident in electron powder bed fusion (E-PBF), works on L-PBF have also showed some control over microstructure though manipulation of the scan strategy and therefore the melt pool geometry [9,10]. This exact manipulation is done through the altering of the solidification velocity and the thermal gradients, which has been shown to be strongly linked to processing parameters [11,12]. Considerations in L-PBF also need to be made for the residual stress. Various works have looked into residual stress using a variety of methods including neutron diffraction experiments [13] and finite element simulations [14], with works showing a relationship between scan strategies and the resulting residual stress.

One new set of materials that have recently gained interest in AM are Fe-Si alloys which are an important alloy within soft magnetic steels that are primarily used in magnetic applications. Using L-PBF the hope would be for a reduction in hysteresis and eddy current through the leveraging of complex geometries, fine control over microstructure, and the utilization of other alloys (i.e. Fe-6.5Si wt. %) considered too brittle for traditional rolling methods. Currently however, Fe-Si steel has yet to see full material characterization with AM. This work specifically, is looking to leverage thermal-mechanical modelling to outline an understanding of both the resulting differences in as-printed microstructure that result based on differences in conditions, and look at how induced plastic strain can lead to differences in abnormal grain growth that have been observed during annealing in thin walled Fe-Si samples that have been produced using different scan strategies. Therefore, this work looks to:

- Analyze the differences in microstructure between as built and annealed microstructure produced using different scan strategy and look at how general crystallographic features may be leading to differences in abnormal grain growth between different scan strategies.
- Leverage thermal models to explain how differences in scan strategy may result in different microstructures in the as-built samples.
- Utilize thermo-mechanical models to make an assessment as to how the scan strategies may be affecting accumulated plastic strain that may be contributing to differences in the rate of abnormal grain growth.

# CHAPTER 2: LITERATURE REVIEW

This chapter will review the previous work presented in the literature that is relevant to the study conducted in this thesis. Section 2.1 will address the development of soft magnetic Fe-Si alloys for AM and the traditional methods used to influence abnormal grain growth of the Goss {110}<001> texture. Section 2.2 will discuss the laser powder bed fusion (L-PBF) process, the effects of processing parameters and previous work relating to parameter development. Section 2.3 will look at the effects of different scan strategies on microstructure and residual stress while section 2.4 will discuss literature surrounding solidification and its effect on microstructure. Finally, section 2.5 will look at different attempts at modelling the AM processes

## 2.1 Soft Magnetic Steels

Soft-magnetic steels play a large role in a variety of industries and find their primary application in transformer cores and electric motors which accounts for nearly half of the global consumption of electricity [9]. Therefore, there is of large interest to see the continued reduction in power losses within these applications through improvement of material properties and application geometry.  In General, the performance of these materials are measured based on the permeability $\mu = B/H$ which should be as high as possible. Here $B$ is the magnetic flux density and is usually defined as the force exerted on a moving charged particle. $H$ is the magnetic field intensity and is defined as the strength of the field of force [15].

Under dynamic and ac application the $B - H$ hysteresis loop is important for understanding energy expenditure for soft magnetic steels. An example of a hysteresis loop is given in Figure 1 and can be seen as a plot of $B$ and $H$. If one were to apply a magnetic field $H$ of increasing intensity, they would find that $B$ would increase from initially zero until it reached the Induction saturation of $B_s$. Afterwards decreasing the magnetic field back to zero does not result in a magnetic flux that goes back to 0. Instead the magnetic dipoles in the material resists the change in magnetization and instead become maintaining their magnetization direction, now obtaining a residual induction ($B_r$). To reduce the induction back to zero therefore requires applying a negative magnetic field. The coercive force ($H_c$) is the applied negative magnetic field at which the induction is zero. Continuing

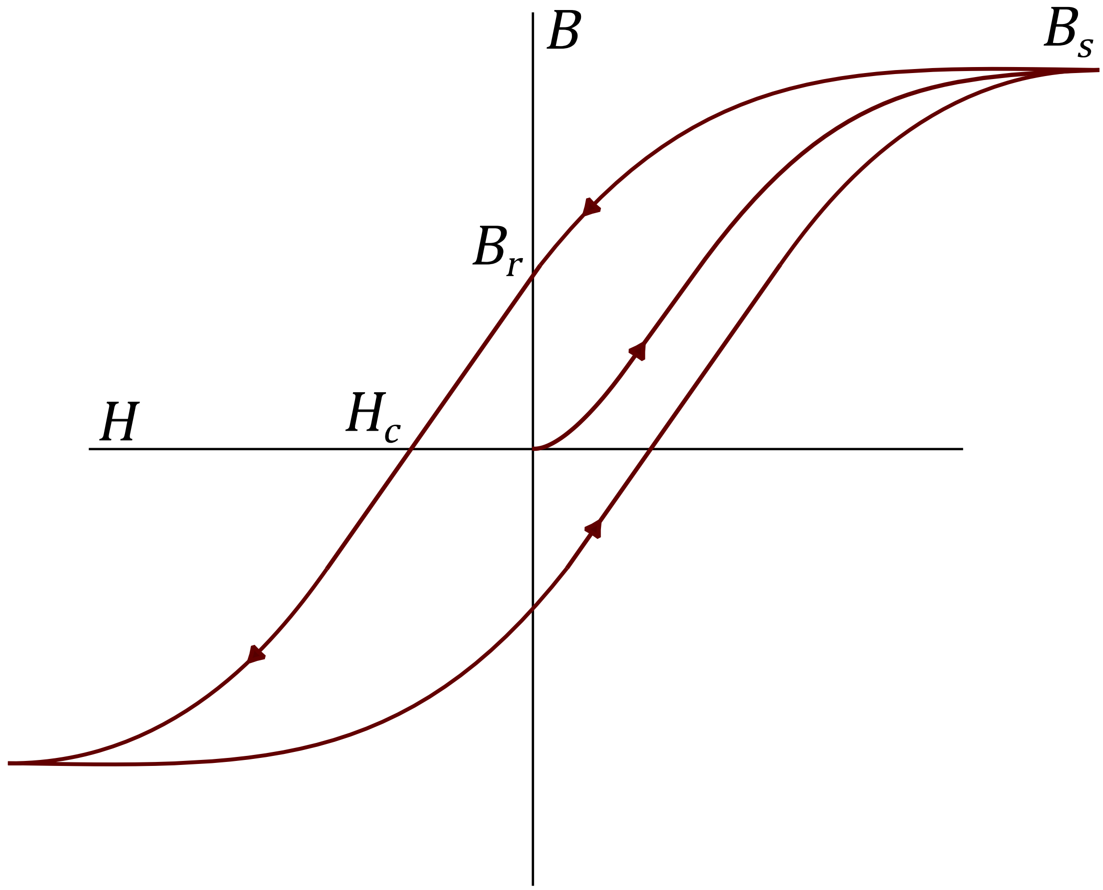


Figure 1 Example of a hysteresis loop

to follow the hysteresis loop eventually one will hit saturation inducting again except in the negative direction, at which point on reduction and reversing of the magnetic field results in a similar trend as previously described. Under an ideal material the hysteresis loop would be as thin as possible and there would be no residual induction after returning the magnetic field to zero however due to resistances in the change in induction this is never the case and therefore results in what are called hysteresis losses. Hysteresis losses are calculated by taking the area of the hysteresis loop such that the hysteresis losses are given as

$$P_h = k(A_h)$$

where $A_h$ is the area of the hysteresis loop. Therefore, a material that minimizes hysteresis losses is one that can reach $B_s$ easily with a minimal $H$ applied where the value of $H_c$ is small. Hysteresis losses are usually minimized through optimization of alloy chemistry and microstructure.

A second form of losses however needs to be considered. Eddy current loses occur from the generation of a magnetic field in the opposite direction of the applied magnetic field that is induced by the changing magnetic flux within the material. The losses due to eddy currents is given as

$$P_e = \frac{\pi^2 t^2 B^2 f^2}{\rho^2}$$

where $B$ is the maximum induction and $\rho$ is the volume resistivity. Overall, these eddy current loses make up a large fraction of the core losses within soft magnetic steels and are highly dependent on the geometry of the device [16].

AM is appealing for the production of soft-magnetic steels due to the complex geometric and microstructural control which is necessary to see further reduction in hysteresis and eddy current losses and for its potential to produce devices using alloys with up to 6.5 wt.% silicon, which are usually too brittle to produce using traditional methods [17,18]. There has been various works in literature that have evaluated Fe-Si alloys for AM. For instance, Garibaldi et. al. [19] in 2016 first demonstrated the possibility for the production of soft magnetic steels in L-PBF. The work produced cubes using high silicon Fe-

6.9Si wt.% and reported the formation of an elongated grain structure in the build direction. Formation of a fully ferritic BCC microstructure with no indication of ordered phase formation was reported which was attributed to the fast cooling rates. Porosity was noted to form when energy input was between 70 J/m and 280 J/m while crack formation occurred between 280 J/m and 560 J/m energy input. Further work by Garibaldi et. al. [20] looked at the magnetic properties of L-PBF produced soft magnetic steels. The work demonstrated a relationship between laser energy input and the reported total power losses where lower losses occurred in samples produced at 280 J/mm compared to samples 140 J/mm due to decreases in porosity. Further increasing the energy input from 280 J/mm to 420 J/mm resulted in a weaker crystallographic orientation in the <100> easy magnetization direction and therefore and increase in hysteresis losses. Work by Plotkowski et. al. [9] showed the effects of scan strategy and geometry on influencing power losses in L-PBF soft magnetic steels. In the work various thin walled samples of thickness ranging from 400 to 1000μm, bulk geometries, and scan rotations were tested. Results showed that thinner geometries and microstructures with increased fiber texture more aligned with the <100> easy magnetization direction resulted in lower eddy current and hysteresis losses respectively. The work also linked differences in predicted thermal gradient due to scan strategy to the microstructure seen in thin wall samples.

One step that will likely be important in the production of soft magnetic steels under AM is an annealing step to increase grain size. While AM is fortunate enough to have in most cases dendrites grow preferentially in the <100> easy magnetization direction, AM generally produces grains that are smaller than the optimal grain size of ~1mm [16] which helps minimize hysteresis loses. Thus, an annealing step will be necessary to increase grain size to further improve the magnetic properties. Few works have currently looked at the effects of annealing AM produced soft magnetic steels [9,18,21], however looking at traditional soft magnetic steel production may give an idea to the grain growth phenomena that is occurring during annealing of AM soft magnetic steels.

Under traditional rolling production techniques a multistep process is utilized, that is designed to encourage the formation of abnormal grain growth of Goss {110}<001> oriented grains in the rolling direction which are known to result in excellent magnetic properties [22,23]. The process starts first with a continuously cast Fe-Si alloy sheet that is then hot rolled, hot band annealed, and cold rolled. Next a decarburization step (i.e. primary annealing) at ~850°C is done followed by a secondary annealing step at 1100-1200°C [22]. In general, it is believed that the hot-rolling step encourages the formation of the Goss oriented grains, while hot band annealing encourages further growth, and cold rolling further deforms of the Goss texture. The primary annealing step (~850°C) results in primary recrystallization of grain structure and the nucleation of some Goss oriented grains. Here grain growth of non-goss grains will be inhibited due to the existence of AlN or MnS particles that pin grain boundaries [16,24,25]. During the secondary annealing step (1100-1200°C ) the particles inhibiting grain growth dissolve and the Goss oriented grains grow selectively at the expense of other grains [16,23,25]. There is however no general consensus on the exact cause of abnormal grain growth in Fe-Si alloys other then it primarily occurs in the Goss {011}<001> texture [22,26–34] when following the traditional production processes mentioned previously. Various cited explanations exist such as the abnormal grain growth occurring due to certain coincidence site lattice (CSL) boundaries that exhibit higher mobility/energy [29–31], or the presence of a driving force for grain growth within certain grain orientations due differences in internal energies between unstrained and strained grains that result during the cold rolling process[32–34].

Despite the lack of consensus on exact mechanisms, in general it is believed that the growth of abnormal grains follows similar mechanisms seen in primary recrystallization [35]. This means that in general the growth of abnormal grains will be affected by grain misorientation, size and strain energies [36]. Currently within AM there has been very little characterization on the effects of microstructural variations on the annealing processes within soft magnetic steels. This work particularly, looks to focus on how differences in scan strategies within the L-PBF process will affect the resulting grain growth seen during annealing of soft magnetic steels.

## 2.2 Laser Powder Bed Fusion Process

Laser Powder Bed Fusion is a standard terminology for additive manufacturing defined by ASTM 52900 [37]. Under this process powder is spread across a substrate with thicknesses usually ranging from 20-100 μm. A laser is used to then melt the powder based on a 2d projection that is extracted from a horizontal “slice” of a 3D CAD model. Many repeated additions of powder layers and melting of these powdered layers based on “slices” from the 3D CAD geometry results in a complete near-net shape part representing the given 3D CAD geometry.

While L-PBF has often been sold on the concept that the process of constructing complex geometries is essential "free" when compared to traditional subtractive methods due to L-PBF's better buy-to-fly ratio and potential time savings, however due to the complex transient weld pools that occur within the L-PBF process, careful planning must be considered regarding the selection of processing parameters (*i.e.*, laser power, laser velocity, hatch spacing, scan strategy, etc.) to obtain defect free parts with consistent and desirable microstructures [38]. In laser welding which shares many similarities to L-PBF, well outlined processing maps to obtain proper mechanical and material properties have been developed based on the geometry and stability of the melt pool [39]. Likewise, processing maps have been utilized in AM to outline appropriate processing ranges [1]. Usually the development of these maps involves the printing of a large array of cubes with different sets of parameters. A case example of process design would be for instance changing the laser power and speed and then presenting a range of parameters that produce defect free, high density parts [40]. However, changes in geometries make these processes maps difficult to utilize due to resulting changes in melt pool dynamics that can result, thus changing expected defect formation and microstructures [12,41]. These works showed that additive manufacturing requires a much more detailed understanding of solidification properties and thermal and residual stresses.

## 2.3 Scan Strategies

The scan strategy plays an important role in influencing the resulting microstructure, and residual stresses within AM parts. There are a variety of scan strategies that are standard on most L-PBF machines. These include raster, island or spot melt scan strategies [1]. In relationship to microstructure formation, work by Thijs et. al. showed under L-PBF using the alloy Ti-6Al-4V, how using a unidirectional raster scan resulted in an epitaxial grain structure that was tilted at 19 degrees away from the build direction while for a raster scans rotated 90 degrees each layer resulted in the formation of a more equiaxed grain structure [42]. Further work for island scan strategies showed a slightly more isotropic equiaxed grain structure when compared to the raster scan rotated 90 degrees each layer [43]. Dehoff et. al. showed on demand texture control demonstrating the ability to actively switch between equiaxed and columnar grain structures by changing from a raster scan strategy for columnar grains to a spot melt scan strategy for equiaxed grain structure in E-PBF [44]. Further work has demonstrated the advantages of fine grain control in AM to produce components that experience complex loading conditions such that they benefit from containing both isotropic equiaxed grains and anisotropic columnar grains at specific locations within the part based on loading conditions [45].

Scan strategy however does not just affect microstructure. Due to the cyclic rapid heating and cooling in AM, considerations relating to the thermal stresses and accompanying residual stresses are important not only for avoiding defect formation such as cracking, but for also maintaining part geometry. Overall, thermal stresses are stresses induced by changes in temperature gradients locally within a material due to the laser scanning processes. Residual stresses are stresses that occur after a full cycle of heating and cooling due to localized temperature gradients from the laser scanning process that causes the local material in the part to undergo thermal expansion, locally seeing an increase in stresses until plastically yielding, and then shrink after cooling while retaining a certain amount of plastic strain due to the previous yielding.

Scan strategies are of important consideration in controlling the residual stress due to the effect scan strategies can have on the temperature gradients and microstructure formation. For example, Figure 2 demonstrates the effects scan strategies can have on residual stress. In Figure 2 thin wall geometries 0.5mm in thickness show buckling in different directions based on scan strategy. Here the use of a unidirectional raster scan strategy (*i.e.*, Longitudinal Raster Scan) bowed the samples outward while a raster scan strategy rotated 67 degrees every layer (i.e. 67° Raster Scan) caused the samples to bow in. In literature, Carter et. al. [10] demonstrated how the island scan strategy utilized in their experiments influenced the occurrence of ductility-dip cracking which occurs from localized reduction of ductility in the material thus leading to cracking when exposed to the buildup of residual stresses that commonly occurs in AM parts. In printed cube samples using an island scan strategy they identified cracking primarily occurring at the fine grain regions that formed at the interface of each island scan. They showed this cracking could be mostly avoided by switching to a simple raster scan strategy. Likewise, work studying the effects of fractal scan strategies [46] showed a change in crack morphology based on scan strategy, where island scan strategies saw crack formation primarily parallel to the scan direction,

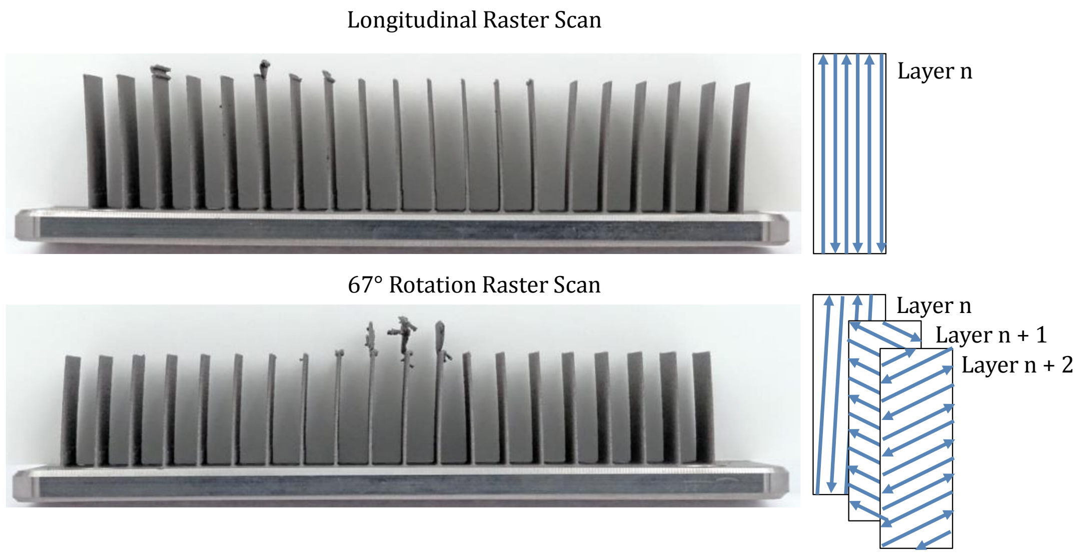


Figure 2 Demonstration of different resulting residual stresses that result from using a longitudinal raster scan, where samples bow out versus a raster scan with a 67° rotation where samples bow in.

where for the fractal scan strategies, while cracking was noted to follow a predictable pattern linked to the resulting thermal profile's effect on residual stresses, the cracks did not follow the scan vector lines unlike the cracking in the island scan strategies. The fractal scan strategies were noted however to have an increase in bulk density (greater than 98 % in the YZ plane) compared to the island scan strategies (less than 97% in the YZ plane) showing a decrease in the number of cracks and therefore likely decreasing the amount of residual stress. Lee *et al.* printing cylinders at 45-degree angles and showed crack formation on only half of the part facing away from the build plate, not supported by the powder. Through simulation of the E-PBF fusion process, they were able to demonstrate that the resulting crack formation was from the buildup of residual stress and through a change from a horizontal to a vertical raster scan strategy, thereby changing the heat transfer properties, were able to decrease the buildup of residual stress and remove the tendency for crack formation [47].

It should be noted however that determining which scan patterns result in lower residual stresses is complex and highly dependent on the accompanying geometry. For example, Ali *et al.* showed through finite element analysis (FEA) for Ti-6Al-4V that raster scan strategies in L-PBF resulted in lower amounts of residual stress compared to island scan strategies and that the rotation of the raster scan strategy (i.e. 45 degree rotation versus 90 degree rotation) resulted in no discernible difference in residual stress levels for cubes with dimensions of 30x30x10mm [48]. Work from Cheng *et al.* for the same processes but using IN718, shows some agreement through FEA simulation of 3 layers of a 6x6mm cube. Island scans in general showed higher levels of residual stress compared to raster scan strategies [49]. However, work from Zaeh *et al.*, using 1.2709 tool steel contradicts the previous presented. Residual stresses here were calculated through x-ray diffraction and instead showed that island scan strategies result in lower buildup of residual stresses compared to a raster scan strategy rotated 90 degrees every layer. It should be noted however that the geometry used by Zaeh *et al.* was a rectangular cantilever geometry with supports thus demonstrating a potential secondary importance in geometry in determining residual stresses making it difficult to outline a specific scan strategy best suited for minimizing residual stresses [50] for all conditions. Further Martin *et al.* justified their use of an island scan strategy for an AlSi10Mg alloy was to minimize the thermal and residual stress build up in their parts [51] further contradicting the idea that one particular scan strategy results in lower residual stresses.

## 2.4 Thermal Gradients and Solidification Velocities

Additive manufacturing due to its rapid solidification conditions may see non-equilibrium elemental partitions and phase selection. Within the AM processes are two important aspects controlling the resulting grain morphology: the nucleation of new solid material within the liquid and the continued growth of existing material. Most often the solidification parameters used to define these processes are the growth rate $R$ (*i.e.*, solid/liquid interface velocity), thermal gradient $G$, and the undercooling $\Delta T$ [52]. Due to the highly transient nature of AM and the resulting complex solidification routines that can result due to a combination of variable scan path and geometry a full understanding of these parameters and their relationships are necessary to understand microstructure formation within AM.

### *2.4.1 Thermal Gradients and Growth Rate*

$G$ and $R$ both find interdependence between each other through the cooling rate ($\dot{T} = GR$) and are strongly influenced by the melt pool geometry and processing conditions. Using welding as a case example Figure 3 [52] shows two weld pools made at a low velocity (a) and a high velocity (b). As the speed of the weld increases it goes from an elliptical shape (Figure 3a) to an elongated tear drop shape (Figure 3b). The hottest region of the weld is at the centerline and the solid region behind the weld pool will see elevated temperatures. For both cases the thermal gradients continue to decrease from the side of the melt pools to the back of the melt pool at the fusion line due to shallower temperature differences, however due to the elongated melt pool in the faster pear shaped weld, the thermal gradients maintain a more consistent direction compared to the slower elliptical weld. As crystals have a tendency to grow in the direction of the steepest thermal gradient, the crystals tend to change growth direction from the edge to the fusion line for the elliptical weld, whereas the pear shaped weld, due to the more consistent direction of the thermal gradients, maintains a consistent growth direction for its grains and sees specific grain orientations stabilize and widen due to the thermal gradient being aligned to the easy growth direction of the grain (given as <100> direction for cubic material).

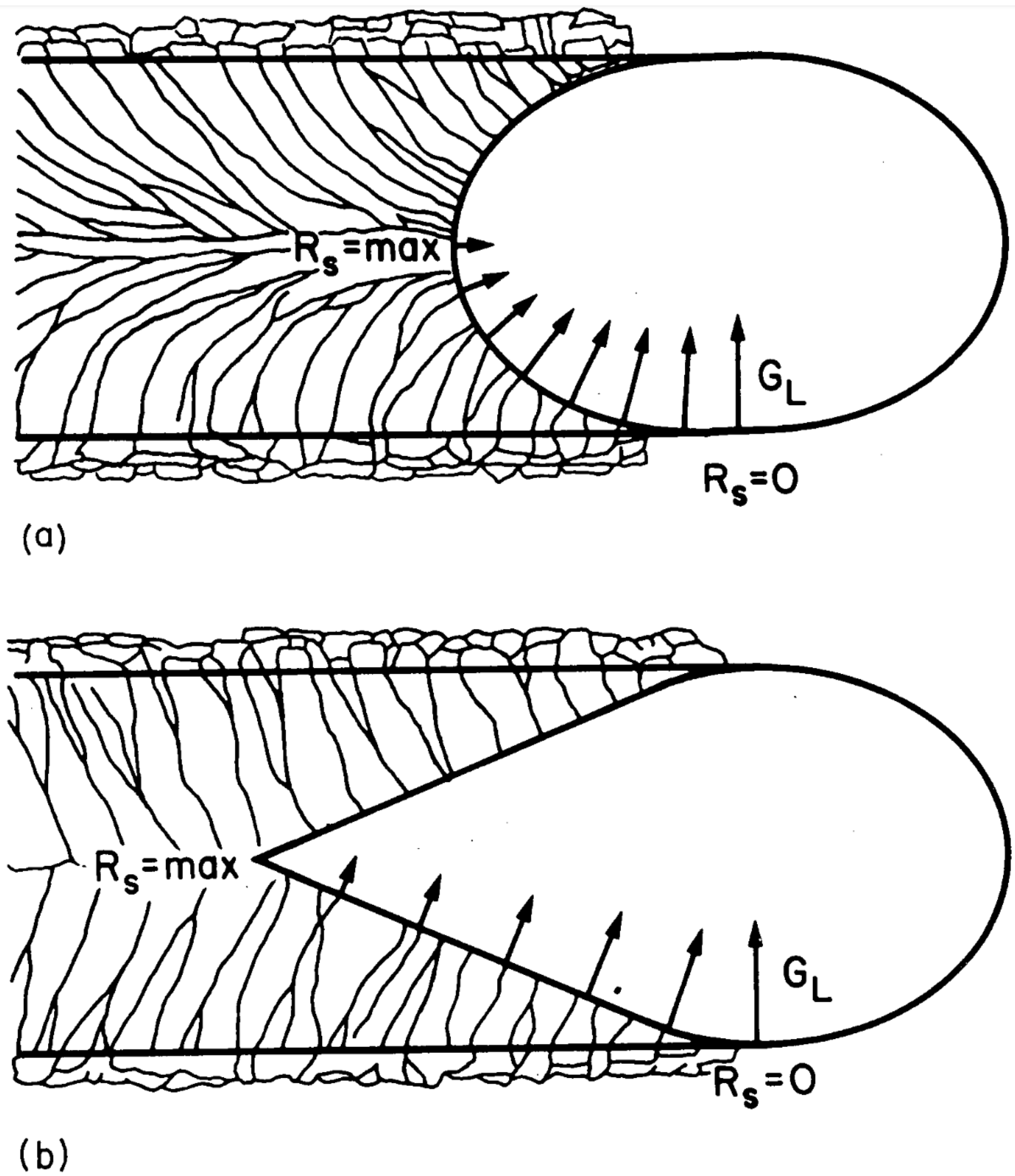


Figure 3 Example of different Thermal Gradients and Growth rates for different melt pool shapes [52]

The growth velocity of the crystals in the two welds in Figure 3 occur such that they keep pace with the weld velocity $v$. Therefore, the growth rate of the solid/liquid interface is given as

$$R = v\cos(\theta)$$

where $\theta$ represents the angle between of the weld direction and the normal direction of the solid/liquid interface. In both weld cases the growth rate is lowest at the sides of the melt pool and highest at the fusion line. The variation in growth rate results in a difference in the buildup of solute at the solid/liquid interface. At particularly high welding velocities it is possible for a high degree of undercooling to occur near the weld fusion line resulting in the nucleation and growth of equiaxed grains while the sides of the weld maintain a columnar structure [36,52,53].

It should be noted here however that the given equation for growth rate above is a simplification for welds purely under steady state conditions, which occurs in AM only under certain conditions. Within AM literature multiple works have looked at how manipulation of the melt pool geometry and processes parameters can change solidification conditions. Raghavan *et al.* and Plotkowski *et al.* demonstrated how a spot melt scan strategy under E-PBF which has a shallower thermal gradient and higher solid/liquid interface velocity compared to the traditional raster scan strategy could result in equiaxed grain formation [54,55]. Likewise, Frederick *et al.* demonstrated how changes in part geometry could alter melt pool condition to result in graded solidification conditions across a given part [12]. Further work from Plotkowski detailed geometry-dependent melt pool solidification conditions in AM through use of a semianalytical heat transfer model, demonstrating that a transition from a quasistatic point source melt pool regime to a quasistatic line source melt pool regime was going to be dependent on processing conditions and material properties [56].

#### *2.4.2 Undercooling*

Undercooling plays an important role in the growth and nucleation of grains. Undercooling is usually defined as the difference in temperature between the liquidus temperature of the alloy in question and the actual temperature. In general, the greater the amount of undercooling the higher likelihood for nucleation to occur. The undercooling is usually composed of four terms [52,57]

$$\Delta T = \Delta T_r + \Delta T_k + \Delta T_h + \Delta T_c$$

where $\Delta T_r$ is the undercooling due to curvature of the dendrites present at the solid/liquid interface. $\Delta T_k$ is the kinetic undercooling and is directly related to the rate at which atoms become attached to the solid. $\Delta T_h$ is the thermal undercooling and relates dendrite growth characteristics to the total melt undercooling [57]. Lastly, $\Delta T_c$ is the constitutional undercooling. It is related to the local change in liquidus temperature due to local changes in the composition [52].

Of the four different undercoolings described above, $\Delta T_k$ and $\Delta T_h$ are considered negligible for AM processes. $\Delta T_r$ only starts to become significant at higher solidification rates and therefore may have some contributions to the undercooling in AM processes. Overall, the most important form of undercooling for determining stability and nucleation of microstructures in AM is the constitutional undercooling. Constitutional undercooling results due to non-equilibrium solidification conditions in which the composition at the interface diverges from the global composition. Figure 4a [53] shows a linear phase diagram turned on its side. Marked is a given composition $C_0$. As $T$ decreases solute is rejected in front of the interface, and a boundary layer enriched in solute forms due to the lack of diffusion. The composition in the liquid at the interface will therefore have a composition of $C_0/k$ as shown in Figure 4a, where $k = C_s/C_l$ and is the partition coefficient. Figure 4b schematically shows the composition based on its distance from the solid/liquid interface. As mentioned previously there is a buildup of solute at the interface that is represented here as the difference in composition from equilibrium conditions $\Delta C_0$. Taking a tangent line at the interface results in a compositional gradient $G_{cl}$. Using the liquidus slope $m_l$ and $G_{cl}$ a relationship can be formed from the plot of temperature versus distance shown in Figure 4c establishing that constitutional undercooling will only occur if the thermal gradient $G < m_l G_{cl}$. Therefore, the constitutional undercooling is highly dependent on the buildup of solute in front of the interface due to non-equilibrium conditions [52,53]. Overall, the exact equations for calculating the undercooling extend

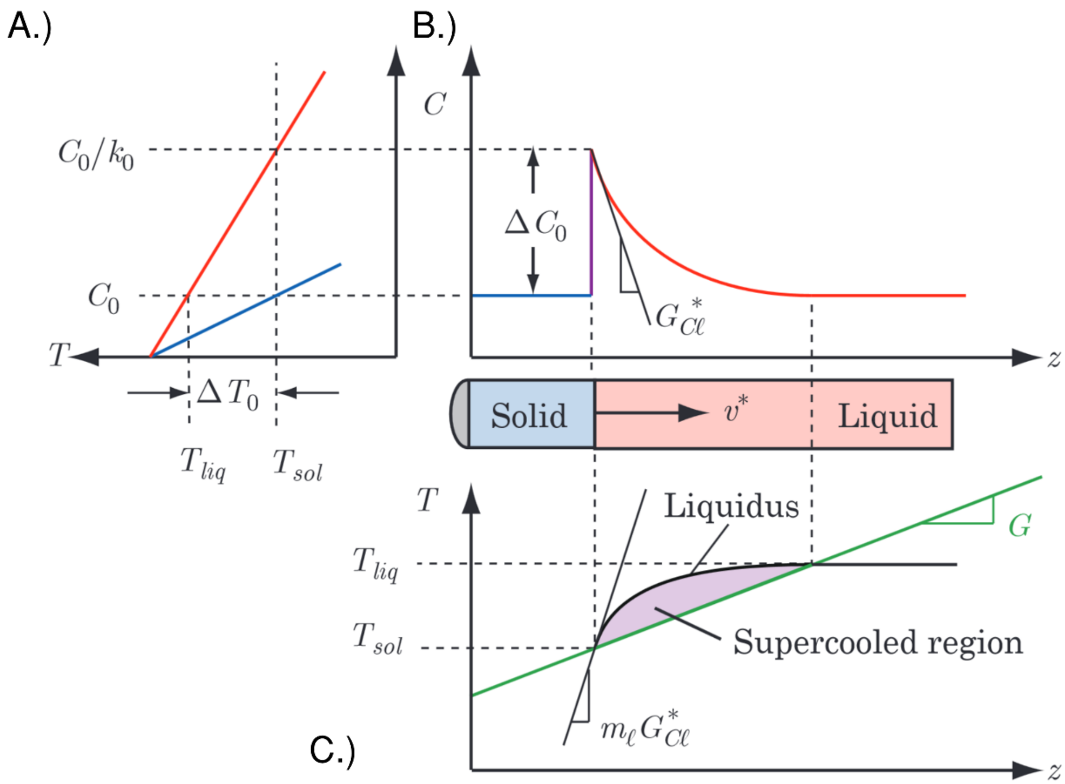


Figure 4 Illustration of constitutional undercooling adapted from [53]

beyond the work performed here, however there are many works that cover how the undercoolings are calculated [57–61].

#### *2.4.3 Columnar to Equiaxed Transition*

Through the utilization of interface response functions which model solidification processes it is possible to model the competition between columnar and equiaxed grains, predicting potential microstructure. Hunt originally modelled the columnar to equiaxed transition for casting processes [62]. The model specifically outlines a columnar front growing in a given thermal gradient $G$ at a specified solid/liquid interface velocity $R$. In front of the columnar front is an undercooled region as described in the previous section for which there is a potential for the nucleation of equiaxed grains. The nucleation and growth of these equiaxed grains is considered using a simple nucleation model that assumes all grains nucleate at the same undercooling. It is possible to use this model to predict whether the equiaxed grains will grow fast enough to block the growth of the columnar grains or whether the columnar grains will out compete the equiaxed grains.

Hunt's model would later be applied to welding conditions[63], and Gäumann would later extend Hunt's model for rapid solidification conditions through integration with the Kurz-Giovanola-Trivedi model [64]. Under AM literature the use of these theories has been adapted to explain microstructure formations based on the solidification conditions. For instance, Dehoff et. al. has used the CET to explain why manipulation of scan patterns allow for manipulation of the formation of columnar or equiaxed grain structures in E-PBF [44]. Fredrick et. al. showed how geometry can influence the formation of columnar and equiaxed grain formation through changes in the thermal gradients and solid-liquid interface velocity [12]. Haines et. al. demonstrated that processing parameters and the number of nucleation sites within the liquid play a more important role then alloy composition for determining CET in E-PBF [11]. Lastly, Plotkowski et. al. used solidification maps to evaluate the potential microstructure formation that would occur in an Al-Ce printed alloy [8].

## 2.5 Thermal and Thermal Mechanical Modelling in AM

Due to the small melt pool and the layer by layer processes, AM is computationally intensive to model and usually requires simplifications in its phenomena. Just for modelling the heat transfer conditions, the transport phenomena consider the exchange of mass, momentum and energy, which involve considerations for conduction, radiation, phase transformation, and fluid motion which in itself can include considerations for the bouncy, Marangoni flow, capillary forces, and recoil pressure. Further considerations have to also be made if one wishes to model the microstructure or residual stress. The choice of which phenomena to model will be depend greatly upon the problems trying to be solved and the time available. The least computationally expensive simulations utilize analytical models [55,65–67] and have been used as a way to quickly generate estimates of the of the local thermal history and residual stresses. These models utilize numerous simplifications including simple boundary conditions, uniform material properties, and no considerations for fluid flow, latent heat release during solidification, or heat loss due to vaporization at the surface. These models are primarily used as tools to help in parameter development more so then in developing an understanding of fundamental phenomena within AM.

Numerical models while being far more computationally expensive compared to analytical models, are able to take into full consideration of the phenomena listed above. For instance, powder bed simulations, which are often interested in forming an understanding of the melt pool flow, spatter, and porosity formation [68–71] often take into full consideration of the transport phenomena including the effects of capillary forces, wetting conditions, and recoil pressure that allows these models to capture full detail of how the laser interacts with the metal powder and liquid melt pool. These powder bed models are some of the most detailed and accurate, however due to the number of phenomena being modeled in these simulations only one or two scan tracks can be modeled.

Residual stress models, used here in this work to establish an understanding of accumulated strain within AM samples, requires a certain amount of simplification due to needing to model heat transfer for entire layers and perform thermal-mechanical simulations over multiple layers. Most residual stress models divide simulations between a thermal simulation and thermal-mechanical simulation. While implementation of the thermal model can differ greatly, most thermal-mechanical simulations follow roughly the same procedures, which are application of the thermal history generated from the thermal model to track thermal expansion of material due to localized heating and see how stress and strain accumulate in the model due to thermal cycling. The number of layers modelled in the thermal-mechanical simulations can vary dependent on spatial and time resolution considerations for both the thermal and thermal-mechanical model.

Overall the degree of simplification of phenomena for the thermal model can vary depending on the goal of the residual stress model. Prabhakar et. al. [14] developed a model using Abaqus for gauging deformation in the base plate in E-PBM. Here the thermal model applied a temperature distribution across each layer of the part for a total discretization of 50 layers. The thermal model accounted for the material properties of the powder but did not account for radiation out of the top surface. The simple thermal model allowed for a full build to be modeled and for observation of temperature, residual stress, and distortion changes within the build plate as the build progressed however is unable to account for effects from scan strategy. Work by Zaeh et. al. [50] utilized a similar approach as Prabhakar et. al. to evaluate the distortion in L-PBF printed cantilever beams and also found adequate correlation with their experimental results.

Lee et. al. [68] utilized a thermal model that simulated the scan path for a single layer, utilizing a conduction only model that ignored fluid flow, latent heat release during solidification, heat loss due to vaporization at the surface and temperature dependent material properties. Heat transfer into the powder was not considered, while radiation into the build chamber from the top surface was. The Thermal model here was then applied to each layer of the thermal-mechanical simulation. Scan strategy considerations on heat conditions allowed for an understanding of how differences in the scan strategy effected accumulated stress and strain and allow for a conclusion that hot cracking seen in the experimental parts was attributed to thermal conditions that could be solved by utilizing a different scan strategy. The simulation was repeated with the new scan strategy and shown that it reduced the chances of hot cracking.

As demonstrated by Cheng et. al., residual stress models can go even further than the previous examples taking further into consideration latent heat of fusion, the effects of powder deposition on the resulting heat transfer, and accurate consideration of layer height [49]. Their model was specifically geared at looking at the effects of different scan strategies on the resulting residual stresses. Overall, the model should result in relatively accurate trends due to the high amount of accuracy in modelling related phenomena. It should be noted that this model however was only able to model a few layers due to computational costs unlike the previously described models. Overall, the models described here show the complexity that can be involved when determining which related phenomena to model such that the results generated by such models can lead to helpful conclusion.

# CHAPTER 3: EXPERIMENTAL PROCEDURES AND RESULTS

## 3.1 Experimental

Builds were produced by Oak Ridge National Labs (ORNL) on a Renishaw AM250 L-PBF machine equipped with a 400W pulsed fiber laser. It should be noted that while most systems utilize a continuous laser, the Renishaw AM250 is unique in that it utilizes a pulsed laser system. Therefore, instead of using laser speed, the Renishaw AM250 utilizes a residence time which is the length of time that the laser is on, while point spacing is the distance between each pulse. Full details on parameters are given further down. The powder was a gas atomized Fe-Si alloy produced by Praxair Surface Technologies and had a sieved particle size range of 15-44μm. The nominal composition as supplied from the specification sheet supplied by the powder manufacture is given in Table 1. The geometry were thin rectangular walls of dimension 0.5x30.0x30.0mm. Thin wall geometries were chosen as they are the preferred geometry for reducing power losses and therefore the most likely geometry to be produced under AM. A full image of the build is presented in Figure 5. Two scan strategy were tested that either scanned in the transverse or longitudinal direction of the part. The scan strategies and the parts are presented in Figure 6. Prior to the work that is presented here other scan directions were tested and it was noted that the transverse and longitudinal samples represented the extremes in terms of microstructures and residual stress. All samples were produced with the same parameters and are given in Table 2. A set of samples were annealed for 1200°C for 5 minutes.

## 3.2 Material Characterization

Sample preparation and characterization was carried out by ORNL. As built and annealed samples were mechanically separated, prepared and polished using conventional metallographic techniques. Electron backscatter diffraction (EBSD) was performed on a Zeiss Evo equipped with an EDAX EBSD detector. Further work to characterize microstructure was performed through the use of Matlab and the package MTEX.

Table 1 Nominal Composition of Soft Magnetic Steel

| **Elements** | **Concentration (wt. %)** |
|---|---|
| Fe | Balance |
| Si | 3.0±0.3 |
| C | 0.04 |
| N | 0.001 |
| O | 0.027 |
| Other | <0.10 |

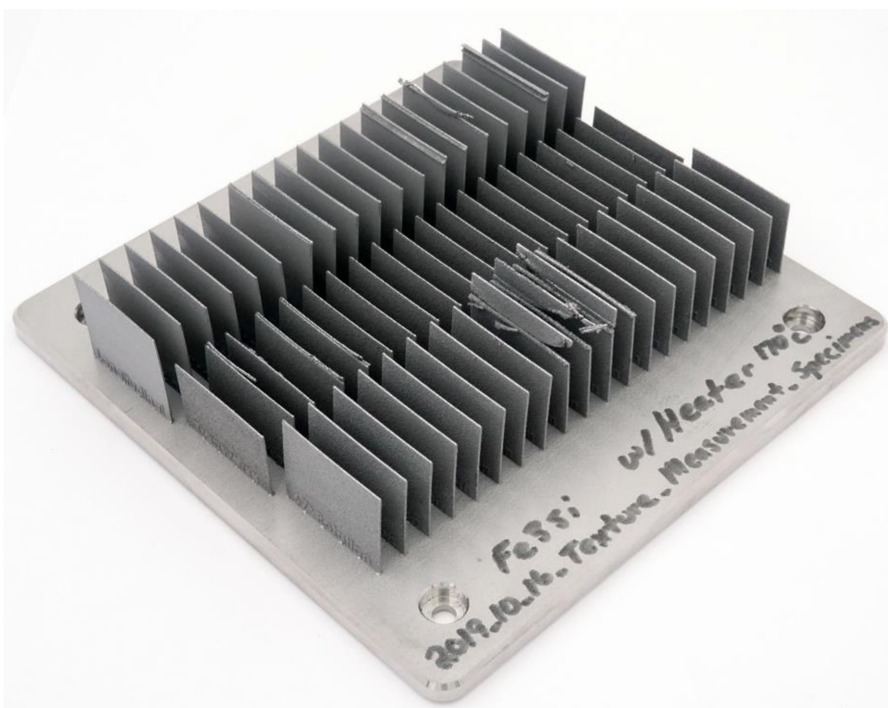


Figure 5 Thin wall samples printed with 0°, 67° and 90° scan rotations and preheat of 170°C

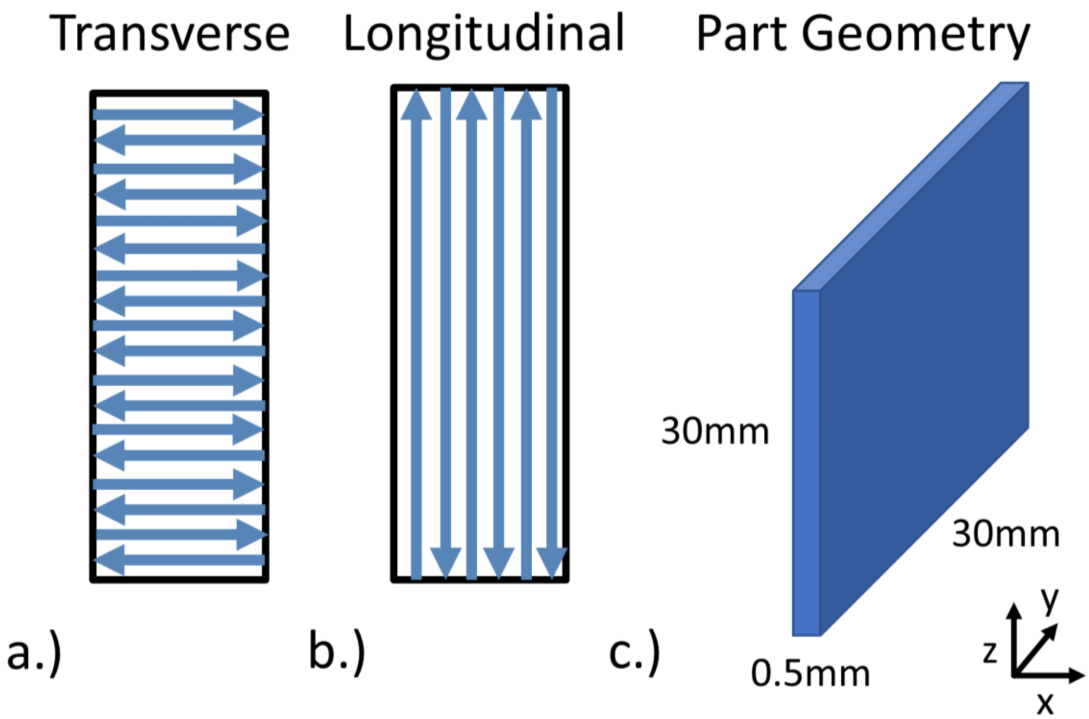


Figure 6 Schematics of the a.) transverse b.) longitudinal scan strategies used in the build and c.) part geometry

Table 2 Table of Parameters used in the build

| **Parameter** | **Value** |
|---|---|
| Laser Power (W) | 200 |
| Residence Time (μs) | 110 |
| Point Spacing (μm) | 75 |
| Hatch Spacing (μm) | 100 |
| Layer Thickness (μm) | 50 |

## 3.3 Weld Pool Geometry

As Discussed previously the weld pool geometry plays an important role in shaping the resulting microstructure. Often thermal models (In this work OpenFoam is used and discussion in detail in Chapter 4) are used to estimate melt pool dynamics due to the complexity of capturing melt pool geometry experimentally. Understanding of the underlying operations of the Renishaw is therefore important. Details over the Renishaw's pulse laser system is given in section 3.3.1 while discussion of modelling of the Renishaw scan strategy is given in section 3.3.2. The melt pool shape from simulation of the scan strategies using OpenFoam is discussed in section 3.3.3.

### *3.3.1 Differences between Pulsed and Continuous Laser Systems*

The Renishaw AM250 utilizes a pulsed laser system instead of a continuous laser system that the majority of other L-PBF machines use. Some work has been conducted noting the differences between a pulsed and continuous laser system [6,72–75]. It has been noted that under pulsed laser systems melt pools showed a "heart-beat" like motion where it expands and contracts between moments where the laser is on and off.  The difference in melt pool solidification also means that the thermal gradients and solidification velocities experienced by pulsed systems are different from continuous laser systems. In general, pulsed laser systems like the Renishaw are noted to be more likely to experience higher cooling rates and a multi-directional solidification front due to the melt pool collapse between pulses [6,74]. Under welding examples using Hastelloy X it has been reported that the occurrence of hot cracking was more common in pulsed laser systems due to differences in melt pool geometry and faster cooling rates causing higher thermal gradients. The differences in melt pool geometry will therefore have an implication on microstructure and potential defect formation. It has also been reported that the microstructure from pulsed laser systems while still epitaxial like most microstructures produced by L-PBF systems, is finer while also more tilted in the laser scanning direction [6]. while producing a microstructure more oriented towards the build direction compared to continuous laser systems [72].

### *3.3.2 Modelling of Renishaw Scan Strategy*

A few aspects about the Renishaw pulse laser system need to be understood before it can be modeled accurately in heat transfer simulations. First, the time between laser pulses varies with spot distance. This is due to the fact that the mechanical galvanometers used to control the laser location have an upper limit on movement speed. It was found by ORNL through analysis of different builds on the Renishaw that the time required to move from one spot melt to the next spot melt is dictated by the spot distance and is given as

$$t = 2 * 10^{-6} + \frac{s * 10^{-3}}{5}$$

where $s$ is the spot distance and $t$ is the time between spot melts. Second the Renishaw will skip two points during a raster scan strategy whenever the laser reverses direction. An example of the point skipping is presented in a representative scan strategy in Figure 7 where the filled in blue circles represent where the laser is on and the dashed circles are the spot melts that are skipped. The laser follows the direction of the red arrows. The reason for skipping spot melts whenever the laser reverses direction is an attempt to maintain consistent heat transfer properties as the region will be hotter due to recent energy input from the laser. Under thin walls however depending on raster direction skipping spot melts can result in large differences in the actual energy density put into the part. For example, on a raster scan performed using the same geometry and processes parameters mentioned in section 3.1, where the raster scan is moving transverse as shown in Figure 6a the number of points being skipped is 1288 of a total 3992 points that could fit into the geometry. For the longitudinal scan strategy shown in Figure 6b only 8 points are skipped of the total 3992 possible points. In general, as will be seen in section 3.3.3, the large number of points being skipped has an effect on the amount of retained heat and thermal gradients in the part.

### *3.3.3 Melt Pool Geometry*

The resulting melt pools from the OpenFOAM simulations utilizing the processes parameters presented in section 3.1 are presented in Figure 8 for the transverse and longitudinal scan strategies. Full detail of the OpenFOAM model is given in section 4.1.1. Comparisons of the OpenFOAM model to experimental results have been made elsewhere

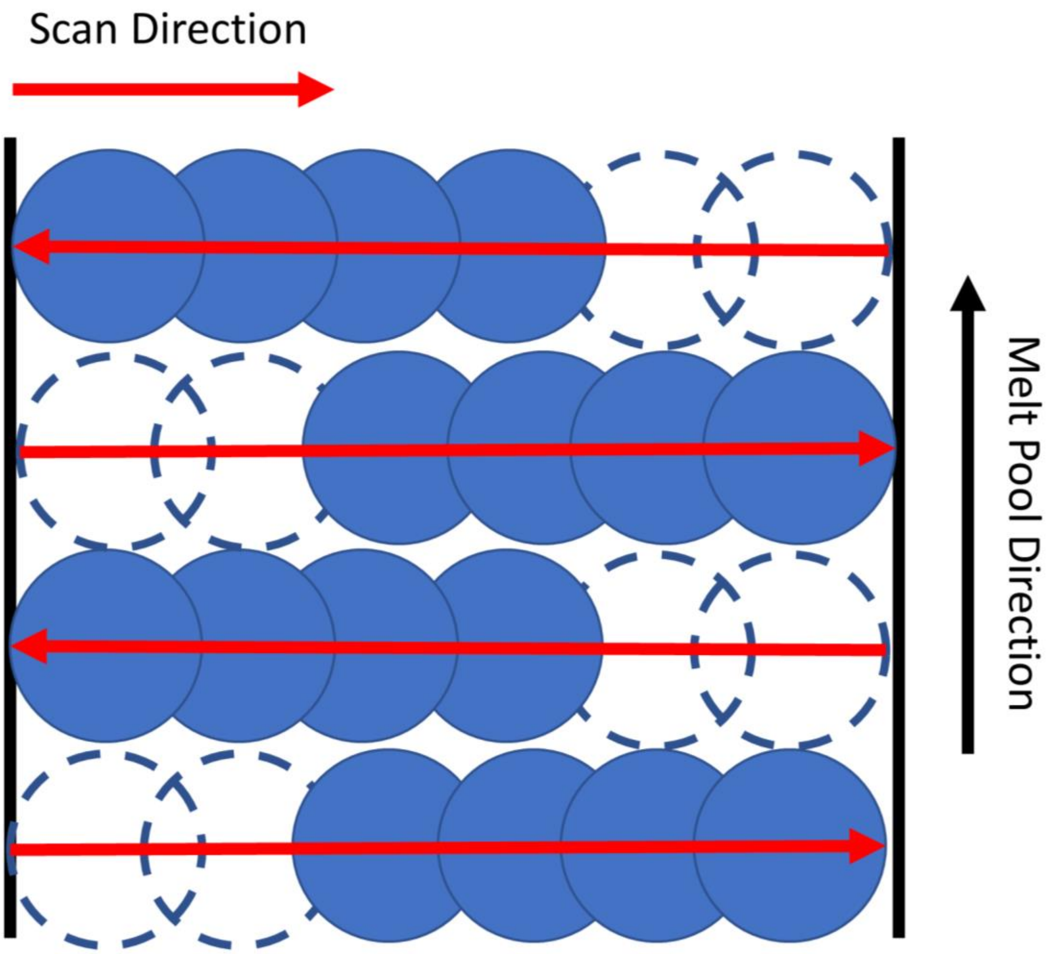


Figure 7 Schematic of the spot melt skipping that occurs in the Renishaw A250

[76].The liquidus line is outlined by a black line and therefore represents the melt pool shape. Figure 8a shows an overhead XY view while Figure 8b shows a side YZ view. The biggest difference is the resulting melt pool shape. For the transverse scan pattern, a large area melt pool forms due to the short scan lines that result in neighboring pulses to often overlap. This melt pool is highly transient as it performs a snake like movement, back and forth across the thin wall. The velocity of the melt pool will vary dependent on the current location of the melt pool. The melt pool thickness in the y direction on the other hand is seen to be rather narrow as seen in the YZ. The longitudinal scan pattern on the other hand demonstrates a more modulated melt pool expected of pulse laser systems instead of the elliptical melt pool expected of continuous laser systems. In total two individual pulses make up the single melt pool. The resulting velocity of the melt pool will be biased strongly towards the lasers. Looking at the side YZ view it is clear that a second spot is forming that will be advancing the melt pool due to the indention present at the front of the melt pool.

The resulting thermal gradients from the two scan strategies are given in Figure 9. Overall the transverse scan strategy appears to show a more constant thermal gradient having one large prominent peak compared to the longitudinal scan strategy. General expectations would be that the Transverse scan strategy due to its quick back and forth scan motion would result in a larger area melt pool that would result in lower thermal gradients. Taking the geometric mean of the thermal gradients it is found that the transverse scan strategy on average does have lower thermal gradients with a mean value of $9.2 \times 10^6$ K/m compared to $10.5 \times 10^6$ K/m. It should be noted from Figure 8 that the longitudinal scan strategy has a significantly higher temperatures ahead of the melt pool compared to the transverse scans likely due to the lack of spot melt skipping resulting in greater heat input. This means that the initial segments of the scan strategy will have higher thermal gradients then later segments of the scan strategies as the background temperature increases and eventually reaches a steady state between the energy put in by the laser and the heat that leaves through the build plate.

A histogram of the solidification velocity is also given in Figure 9. Both scan strategies show a relatively bimodal distribution of solidification velocities that line up with each other closely, however this bimodal distribution is far more prominent in the longitudinal scan strategy. In general, the solidification velocity plays a role in the

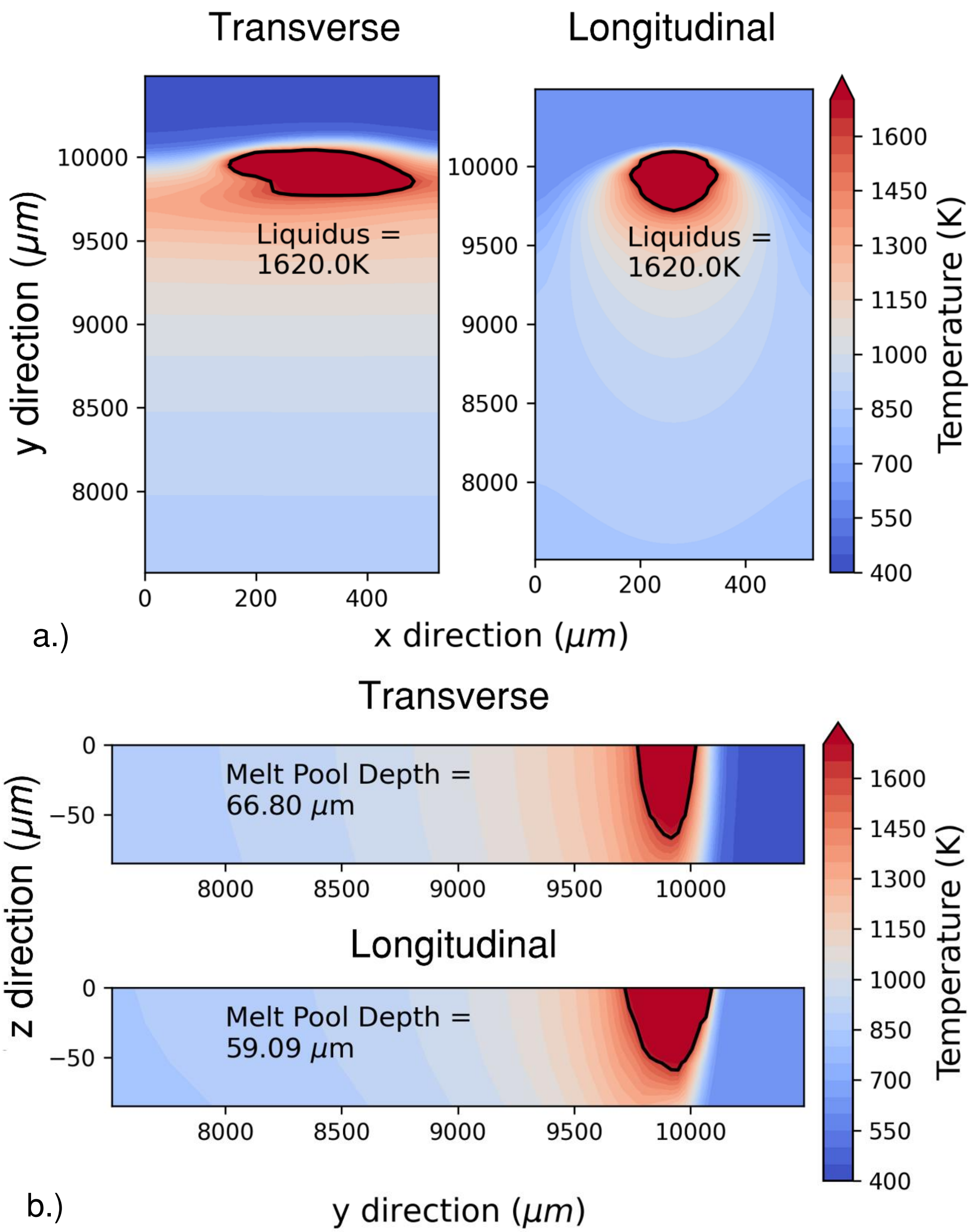


Figure 8 Simulated melt pools from openfoam where a.) is an overhead XY view and b.) is a side YZ view

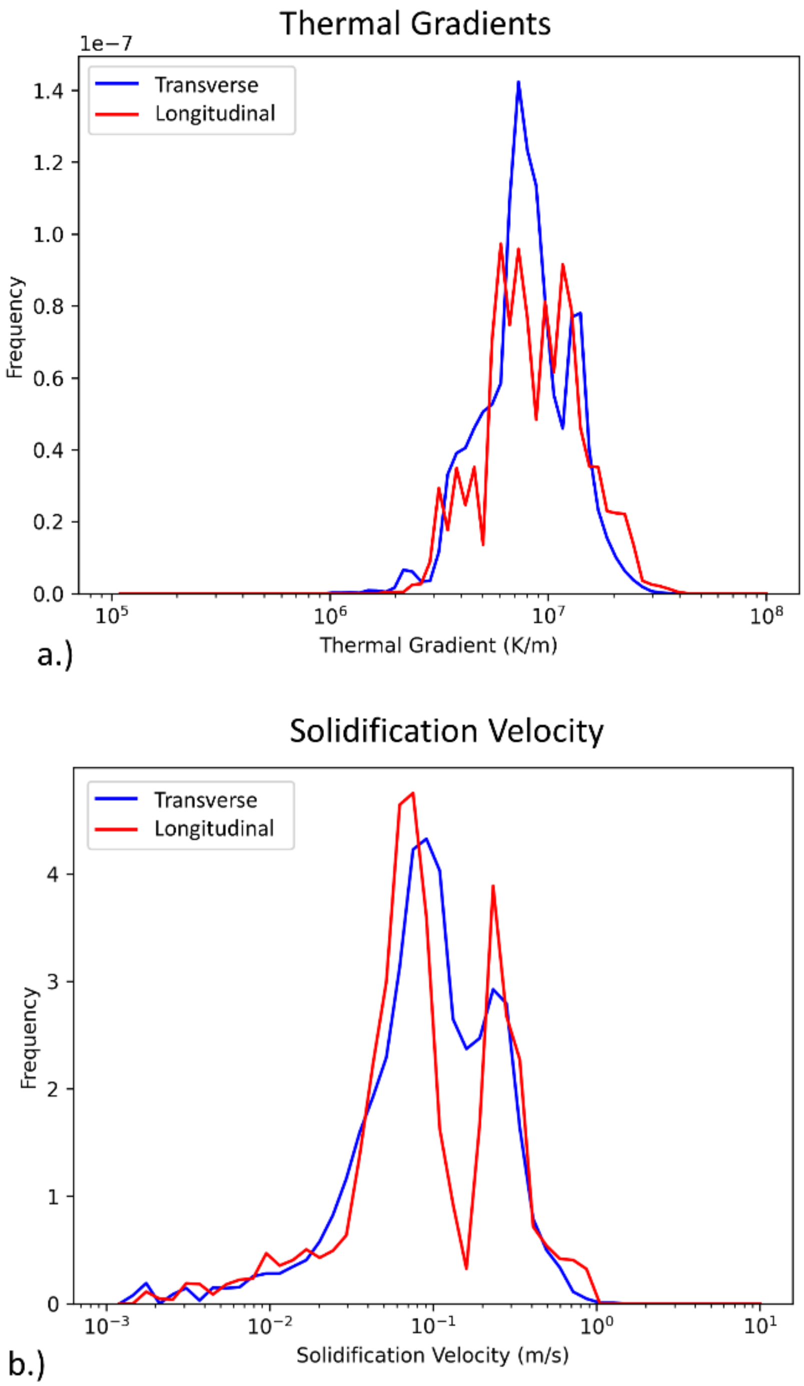


Figure 9 Histogram of (a) thermal gradients and (b) Solidification velocity for the transverse and longitudinal scan strategies

undercooling in front of the dendrite tips, where faster solidification velocity results in a greater chance for the nucleation of new grains.

## 3.4 Microstructure Results

Crystallographic attributes that can be collected by EBSD that are likely to affect grain growth include grain orientation, size and misorientation. EBSD was collected for both the as built and annealed samples to obtain initial observation on these attributes and whether they could be influencing abnormal grain growth during annealing. The as-built microstructure is first presented and discussed in section 3.4.1, while the annealed scan strategy is presented and discussed in section 3.4.2. The potential influences that the grain texture, size and misorientation might have on the abnormal grain growth is discussed in section 3.4.3

### *3.4.1 As-Built Microstructure*

The grain structure and crystallographic texture, obtained from EBSD, for the transverse and the longitudinal as-built samples are presented in Figure 10 both perpendicular (XZ-plane) and parallel (XY-plane) to the build direction. The transverse direction is noted for having larger grains and greater texture compared to the longitudinal scan. Overall the transverse scan for the perpendicular (XZ-plane) has a mean grain diameter of 162.6 μm and texture index of 3.59 whereas the longitudinal scan has a mean grain diameter of 53.3 μm and texture index of 1.17. Looking at the pole figures the transverse direction shows highly textured grains with the grain orientation predominately tilted away from the <100> build direction. The longitudinal scan direction also shows less texture but still a prominent number of grains with a slight tilt away from the <100> direction however not as strongly tilted as the transverse scan strategy.

The indication of texture, evident from the pole figure, in the longitudinal scan strategy should be evidence that no/limited CET occurred such that equiaxed grain formation within the melt pool did not result in blocking the growth of columnar grains, It is possible to plot the CET together with the simulated thermal gradients and solidification velocities from OpenFOAM to show that just a change in scan strategy is not enough to greatly change grain morphology and cause a CET. Figure 11 shows the CET together with

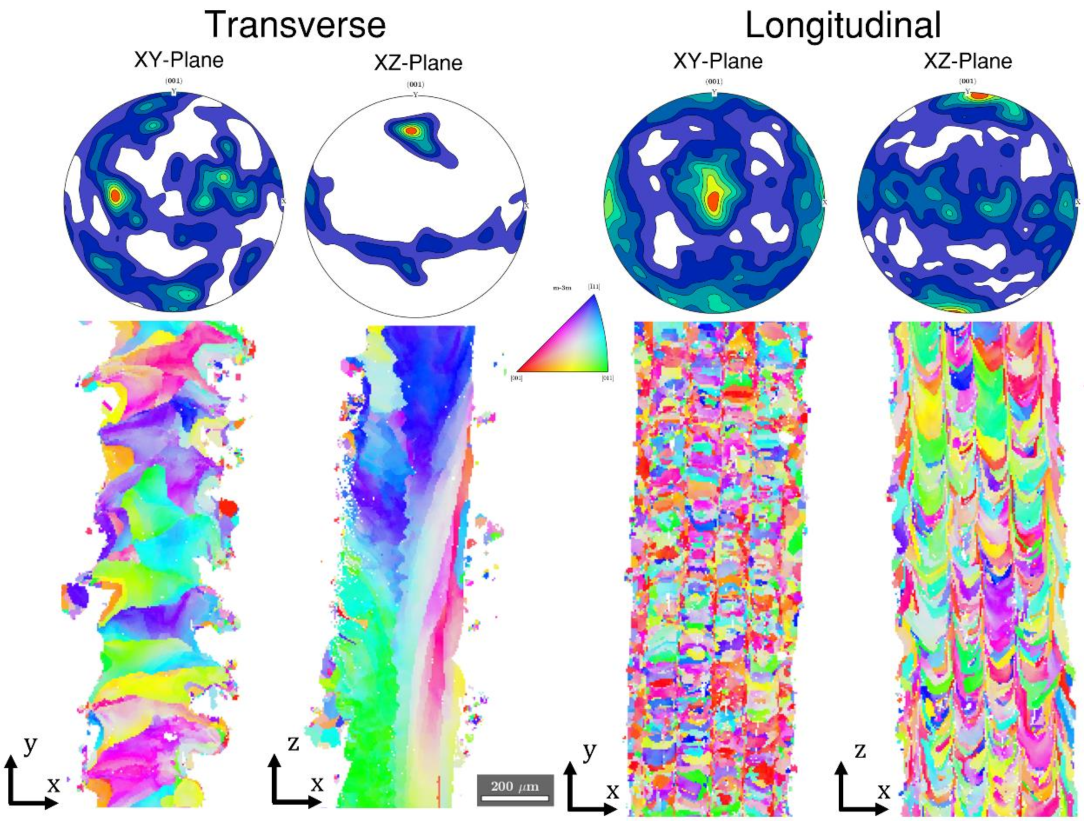


Figure 10 EBSD and pole figures of the as-built transverse and longitudinal scans strategies for both parallel (XZ-plane) and perpendicular (XY-plane) to the build direction

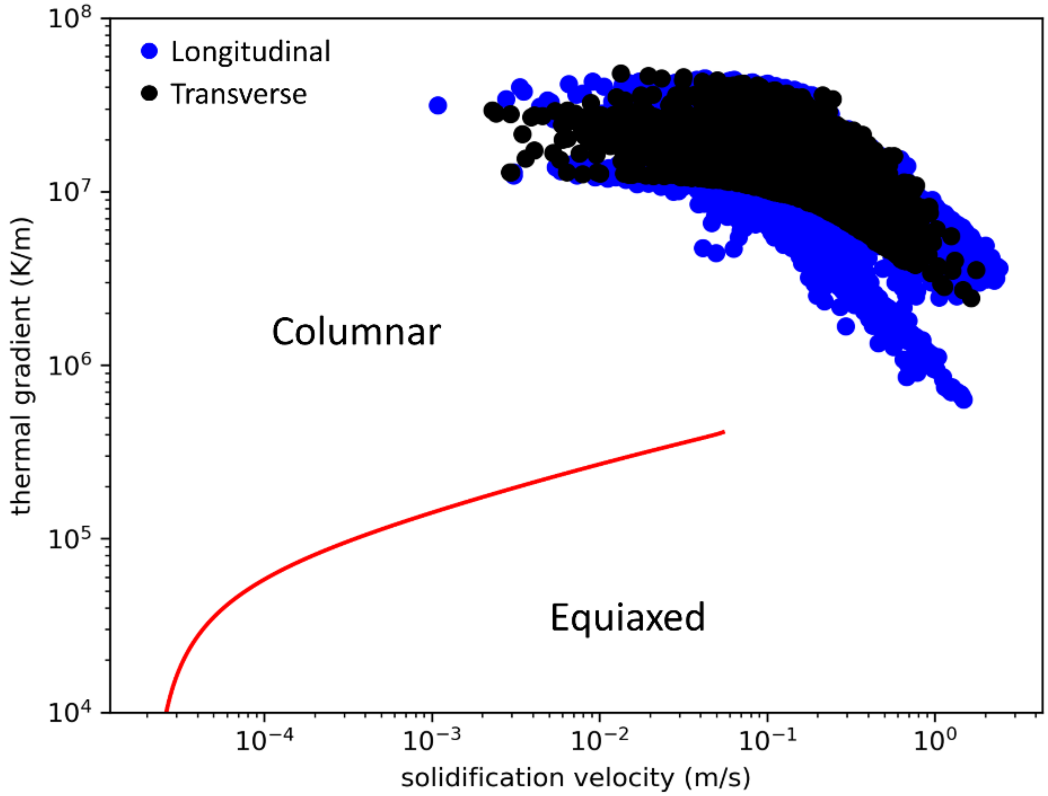


Figure 11 CET of Fe-3Si with Thermal Gradients and Solidification velocity for the Transvers and Longitudinal scan strategies

the thermal gradients and solidification velocity for the transverse and longitudinal scans plotted. The nucleation volume density ($N_0$) used for the CET has been specifically calibrated here to the grain structure of the longitudinal scan strategy under the assumption that $N_0 = 1/d^3$, where $d$ is the grain size. Using the grain diameter listed above from the longitudinal scan strategy, $N_0 = 6.7 * 10^{12}$ $m^{-3}$. In AM processes specifically, the nucleation volume density has been noted to vary between $1x10^{11}$ to $2x10^{15}$ $m^{-3}$ [12,64] dependent on processes and therefore the value calculated here for the nucleation volume is within the expected range. From Figure 11 it should be clear that both scan strategies are far within the columnar region and therefore a CET cannot occur, therefore another mechanism needs to be highlighted to explain changes in grain structure.

The changes in the texture with respect to build direction from the transverse scan to the longitudinal scan can likely be attributed to changes in the preferred dendritic growth direction which is influenced by the thermal gradients. The dendritic growth direction has been known in additive manufacturing to have a significant impact on the local undercooling and nucleation of misoriented grains [54]. In general, sudden changes in the thermal gradient vectors are expected to result in the nucleation of new grains reducing the overall grain size within the part.

A visual qualitative approach for analyzing the effects of the thermal gradients on dendritic growth is through the thermal gradient streamlines and has been used by other works to qualitatively correlate thermal gradients to microstructure in AM [9,77]. Here the thermal gradients from the OpenFOAM simulation were replicated for eight layers by overlaying the thermal gradients of the bottom 50 μm that would not be remelted by the melting of the next powder layer. The buildup of heat with the melting of additional layers was considered not a concern because it was found in the OpenFOAM simulations that the layer would reach preheat temperature in about 15 seconds for a 60 second layer time. The streamlines were produced for 2d planes using the python package Matplotlib's streamline function for the XZ-plane and XY-plane of the transverse and longitudinal scan strategies. The XZ-plane specifically utilizes the thermal gradients in the X and Z directions while the XY-plane utilizes the thermal gradients in the X and Y direction. The results are presented in Figure 12 along with EBSD results as a reference. Looking at the streamlines for the XZ-plane of the transverse scan strategy (Figure 12a) show a more uniform solidification path

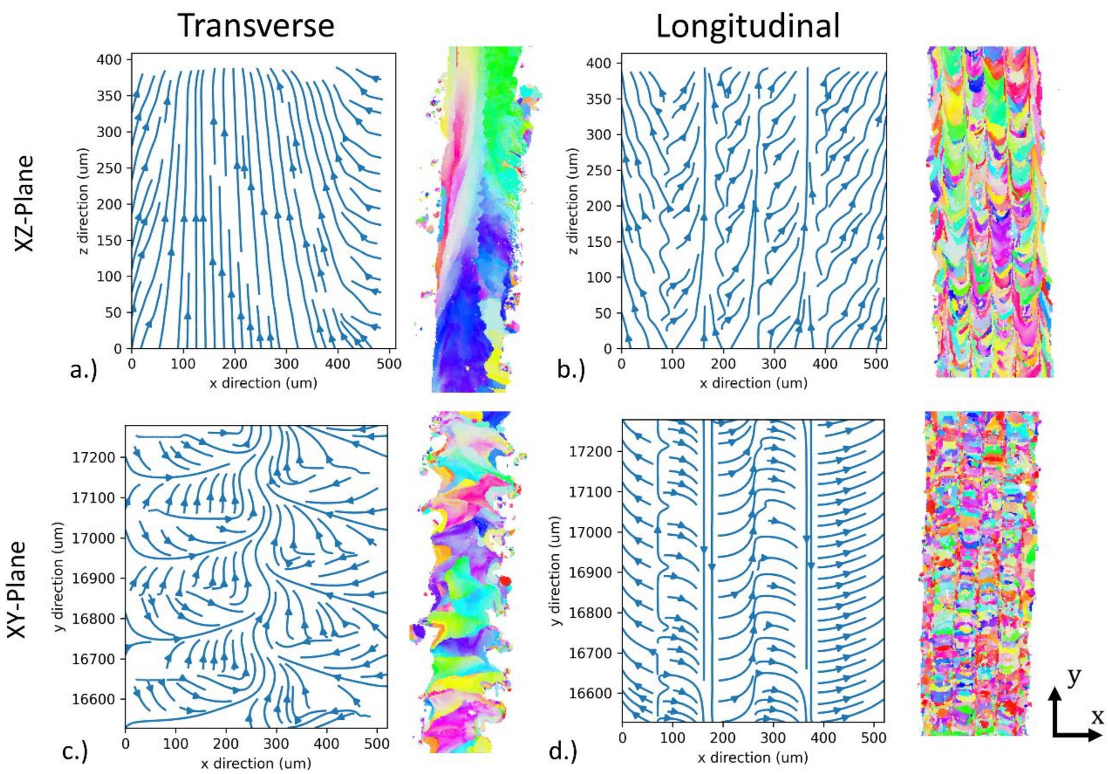


Figure 12 Thermal Gradient Streamlines generated for the Transverse (a and c) and Longitudinal (b and d) scan strategies in the XZ-plane (a and b) and XY-plane (c and d)

which converges gradually towards the center similar to the transverse scan EBSD image. In the XY-plane (Figure 12c) the streamlines undulate back and forth. There are also noticeable regions in which the streamlines are diverging in opposite directions which seem to correlate well to the occurrence of the individual grain segments that are oriented at a slight angle away from the x-direction as seen in the XY-plane EBSD image. The longitudinal scan strategy on the other hand shows more broken streamlines divided into individual columns in the XZ-plane (Figure 12b). Likewise, the longitudinal scan EBSD is noticeably divided into columns that correlate with the number of columns in the streamline. In the XY-plane (Figure 12d) like the XZ-plane the column divisions still persist however most streamlines are further tilted mostly perpendicular from the scan direction therefore likely contributing to the small grains seen in the EBSD. Overall, under the assumption that dendrites grow relatively parallel to the thermal gradient direction and cannot cross a perpendicular thermal gradient, the individual grain segments within these EBSD can likely be explained by sharp divergences or sudden changes in thermal gradient direction that are seen within the streamline

Quantitatively, it is possible to measure the potential influence of thermal gradients on the dendritic growth direction through plotting of the spatiotemporal variation of the direction of the temperature gradient at the solid/liquid interface [78]. The result can be calculated using the given equation

$$\theta = \cos^{-1}\left(\frac{G_z}{G_{resultant}}\right)$$

where $\theta$ is the measure of the angle between the thermal gradient vector ($G_{resultant}$) at the solid/liquid interface and the thermal gradient in the z-direction ($G_z$) that is aligned to the build direction. Similar as before due to the layer height of 50μm, only thermal gradients from the bottom 50μm where plotted as anything above would be remelted. The histogram of the resultant expected dendritic growth direction for the transverse and longitudinal scans are shown in Figure 13. For the transverse scan the thermal gradient is tilted up to 25 degrees away from the build direction and the <100> easy growth. Overall this is in agreement with the pole figures in Figure 10 for the transverse scans which show a textured grain structure that is oriented away from the <100> direction. The longitudinal scan on the

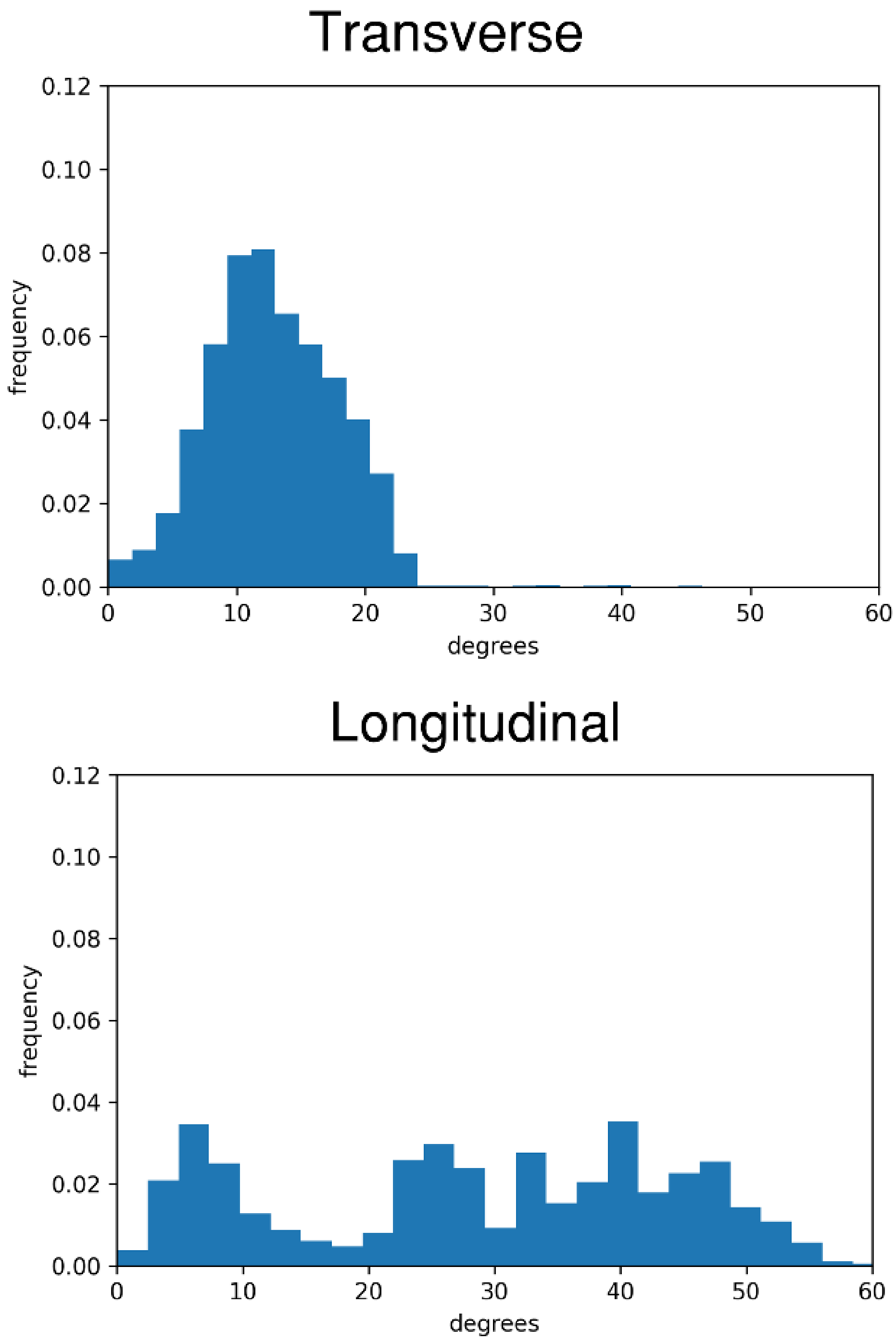


Figure 13 Histograms showing variation in Thermal Gradient direction compared to the build direction

other hand shows a preference in the thermal gradient direction to vary up to 60 degrees from the build direction with a relatively randomly distribution of directions. The growth of dendrites tends to follow the resultant thermal gradient, with specific crystal orientations being preferred known as the easy growth directions as discussed previously. The constantly changing thermal gradient direction therefore results in a constantly changing preferred growth direction, greater competition between different crystal orientations and a greater possibility for the nucleating of stray grains which results in the longitudinal scan strategy having smaller less textured grains comparatively.

### *3.4.2 Annealed Microstructure Results*

The EBSD results from annealing samples for 5 minutes at 1200°C is given in Figure 14 for planes perpendicular (XZ-plane) and parallel (XY-plane) to the build direction. It should be noted that the mounting material has been picked up by the EBSD detector and is seen as a large number of misoriented grains around the actual samples. The difference between the samples and mounting material has been accounted for when calculating the pole figures. The transverse samples saw very little change in grain structure after the annealing, however there are a noted set of striations that have formed in the EBSD for both XZ-plane and XY-plane. These striations could be the beginnings of newly nucleated grains or the growth of prior grains that were not picked up by the EBSD. The pole figures of the transverse scan in the XZ-plane also shows the appearance of new grain directions that were not present prior to annealing. The longitudinal samples on the other hand, saw a large amount of abnormal grain growth that is characteristic of annealed Fe-Si alloys. It also appears that the grain boundaries of the newly grown grains strongly align with the previous weld pool boundaries. It should be noted here that the limited number of EBSD images collected does not allow for a statistically reasonable assertion to be made if a particular grain orientation plays a role in the occurrence of abnormal grain growth as has been reported for traditional processes. Case in point is made when looking at Figure 15 showing a second EBSD image of an annealed longitudinal scan strategy in the parallel (XY-plane) which shows a largely different preferential grain orientation that has grown compared to the grains shown in the longitudinal scan strategy in the parallel (XY-plane) in Figure 14.

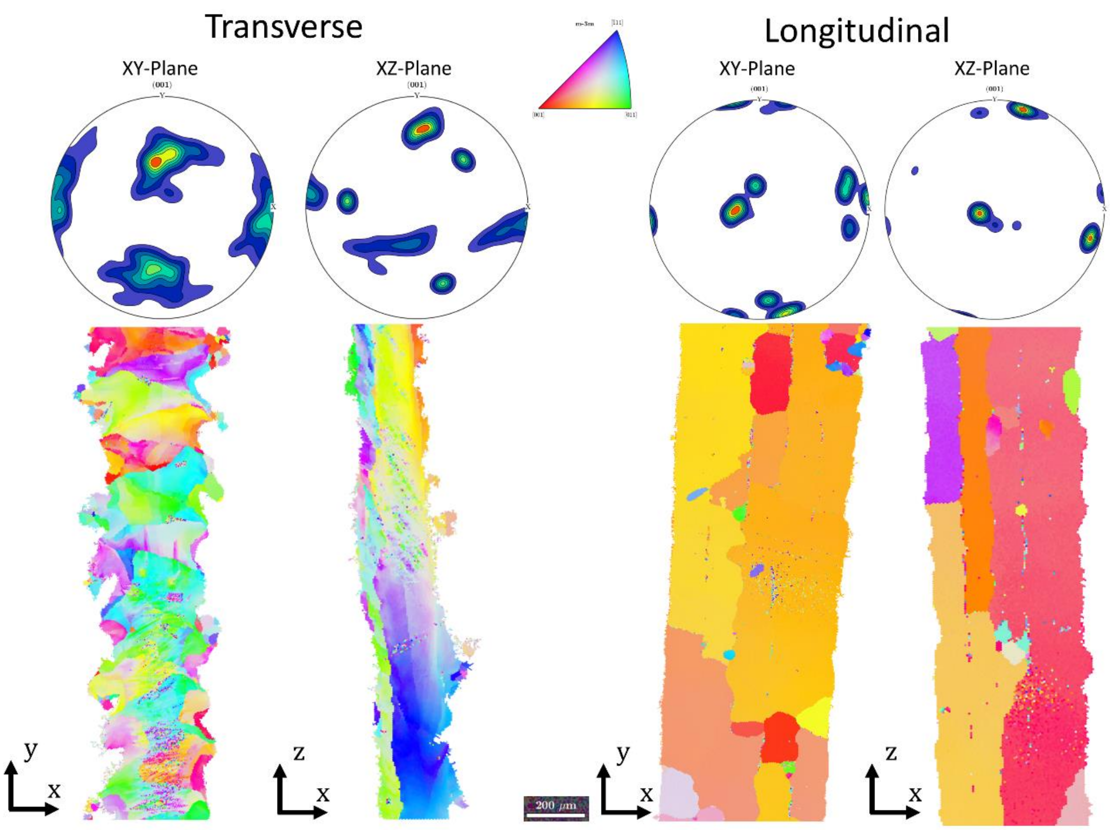


Figure 14 EBSD and pole figures of the annealed transverse and longitudinal scans strategies for both parallel (XZ-plane) and perpendicular (XY-plane) to the build direction

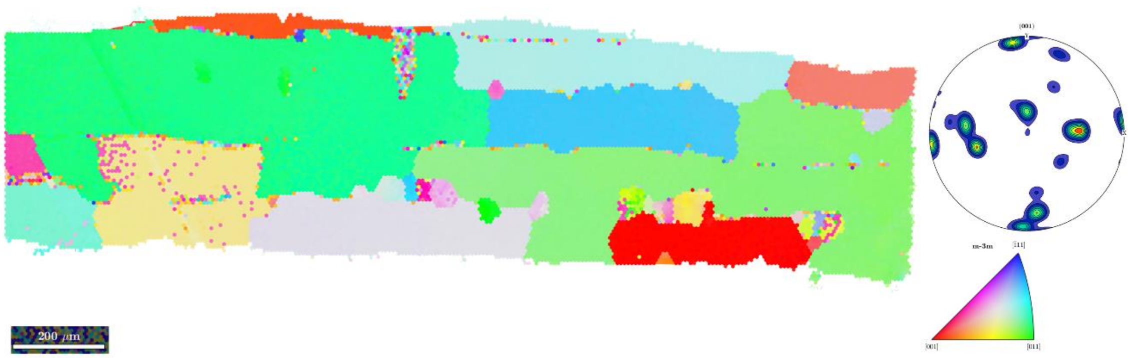


Figure 15 EBSD image and pole figure of an Annealed longitudinal sample in the XY-plane showing different grain orientations

### *3.4.3 Microstructure Factors contributing to Grain Growth*

The driving force for abnormal grain growth ($P_m$) like primary recrystallization is dependent on both the energy at the grain boundaries ($\gamma_b$), which is influenced by the grain misorientation, and the mean grain diameter ($D_M$) [35] such that the driving force for abnormal grain growth is given as

$$P_m = \frac{3\gamma_b}{D_M}$$

From the equation it should be clear that decreasing mean grain diameter and increasing grain boundary energy through increasing grain misorientation should increase the driving force for abnormal grain growth. As mentioned previously the longitudinal scan strategy resulted in a smaller grain size compared to the transverse scan strategy. Calculations of the grain boundary misorientation using the 2D EBSD data shows similar trends and is presented as a histogram in Figure 16 for the transverse and longitudinal scans. Overall, the longitudinal scan strategy has a larger number of highly misoriented grains compared to the transverse scan strategy. On a quantitative basis it can therefore be concluded that there is a very strong likelihood that microstructural differences that occur due to different scan strategies has played a role in affecting the growth kinetics of grains during annealing resulting in abnormal grain growth in the longitudinal samples. It should be noted however that quantitative work still needs to be done to determine the significance of grain texture, size and misorientation. Furthermore, work needs to be done to understand if there is a preferred grain orientation that grows as is seen with the Goss texture in traditional Fe-Si processing techniques. Exact details on the necessary future work is given in Chapter 5. Lastly, the work in Chapter 3 only made conclusions based on what could be observed in EBSD, however due to the thermal stresses caused by the layer by layer processes in L-PBF, the effect of accumulated plastic strain on the abnormal grain growth also needs to be considered, and is discussed in Chapter 4.

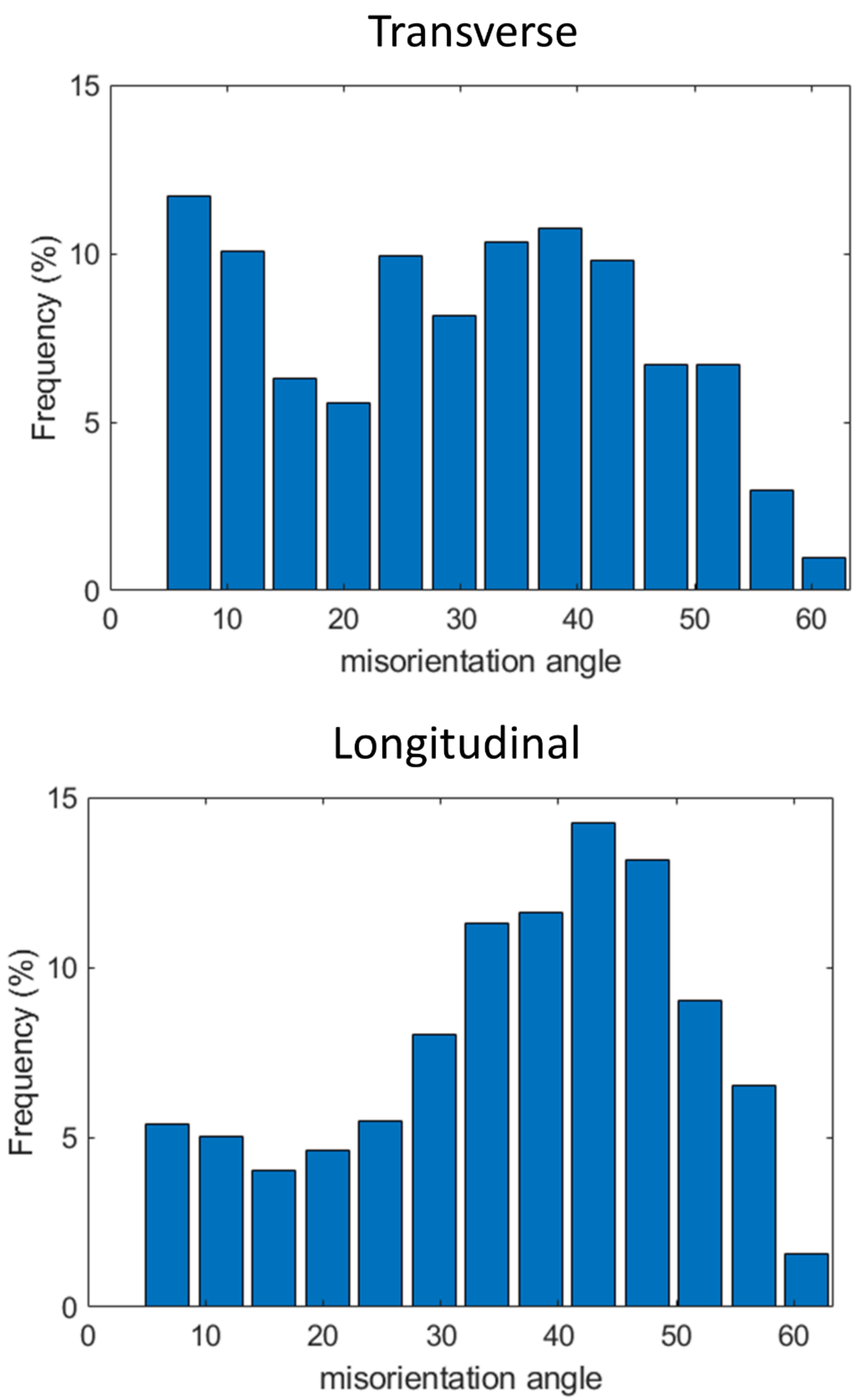


Figure 16 Grain misorientation for Transverse and Longitudinal samples

# CHAPTER 4: THERMAL-MECHANICAL SIMULATION AND RESULTS

## 4.1 Numerical Simulation Methods

When utilizing simulations to help solve a specific problem, due to limited computational resources, one should consider the specific physical phenomena that are necessary, and which can be simplified within their model. For the modelling of residual stresses, work has ranged from modelling phenomena on the macroscale to the utilization of microscale and mesoscale hybrid models as described previously in section 2.5. The work presented here is specifically interested in measuring detailed differences between scan strategies and therefore has opted for detailed modelling of the full scan path. The model is broken into two segments, a microscale thermal model ran in OpenFOAM and a mesoscale thermo-mechanical model constructed in Abaqus. A workflow outlining the individual steps involved in the model is given in Figure 17, with a full description given in the proceeding sections.

### *4.1.1 Thermal Model*

The OpenFOAM simulation captures the full laser scan path including the individual pulses of the laser so that a full understanding on the effects of different scan strategies can be obtained. The OpenFOAM model utilizes a solver originally developed by ORNL and is described in full detail in [76]. Fluid flow was not considered in these simulations to save computation time, because the thermal mechanical Abaqus models mesh resolution would be too coarse to capture differences between melt pools with and without fluid flow. Therefore, the OpenFOAM model used here accounted for conduction, convection from gas flow, and radiation. The governing equation is given as

$$\frac{\partial(\rho c_p T))}{\partial t} = \nabla \cdot (k\nabla T) + S_T + \dot{Q}$$

where the volumetric energy source term $\dot{Q}$ is the heat added to the system by the laser and is modelled by a Goldak heat source [79]. The energy source term $S_T$ is the evolution of

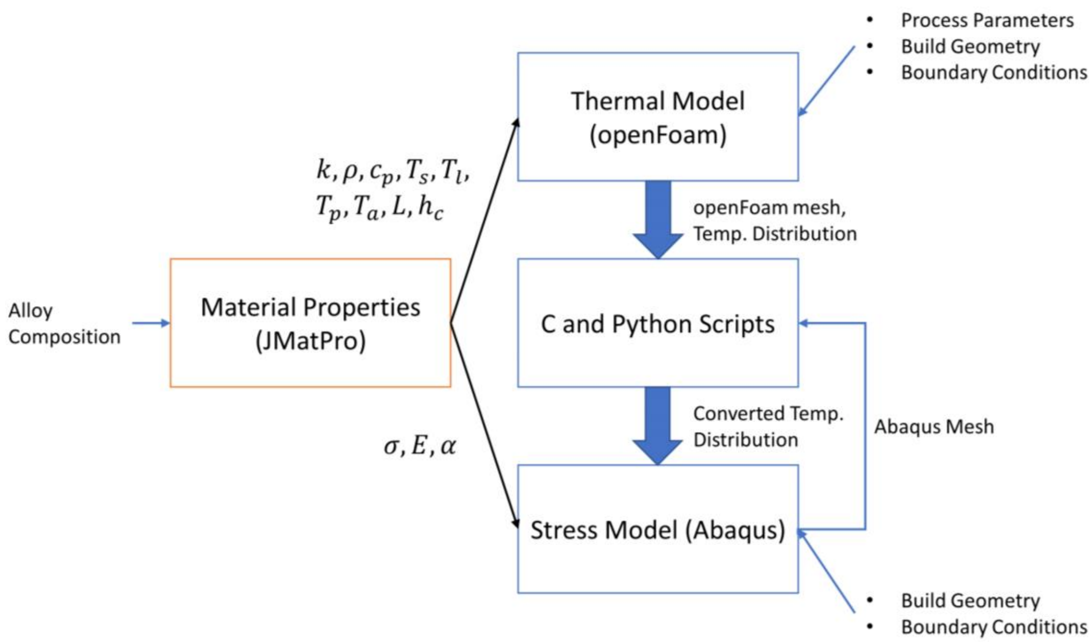


Figure 17 Workflow outlining the steps for modeling the residual stress

latent heat during phase change, $k$ is the mixture thermal conductivity of the solid and liquid, $T$ is the temperature, $U$ is the velocity vector, $c_p$ is the mixture specific heat, $\rho$ is the mixture density, and $t$ is the time. The top surface of the part had a combined radiation and convection boundary condition for consideration of heat losses to the atmosphere. The radiation and convection boundary conditions are given respectively

$$q_r = \varepsilon\sigma(T^4 - T_a^4)$$

$$q_c = h_c(T - T_a)$$

where $q_r$ and $q_c$ are the heat flux from radiation and convection respectively, $\varepsilon$ is the emissivity, $\sigma$ is the Stefan-Boltzmann constant given as 5.67x10$^{-8}$ W/m$^2$, $h_c$ is the convection coefficient, and $T_a$ is the temperature of the atmosphere.

The material properties for density, specific heat, and thermal conduction accounted for temperature dependencies and thus used polynomials expressions for the solid and liquid states. The data for the polynomials were obtained through JMatPro [80] and are given in Table 3. All other material properties with the exception of the emissivity and convection coefficient were also obtained from JMatPro [80] and are given in Table 4. The emissivity was left as the default that is given in OpenFOAM as there is no easy way to determine this value without extensive experimentation that falls out of the scope of this work. The convection coefficient was calculated based on the assumption of free convection over a plate with laminar flow. Using relationships between the convection coefficient, Nusselt's number, Prandtl's number, and Reynold's it is possible to calculate a value for the convection coefficient through the given equations

$$\mathrm{Nu_x} = 0.664\mathrm{Re_x^{\frac{1}{2}}}\mathrm{Pr^{\frac{1}{3}}}$$

$$Nu_x = \frac{hL}{k_g}$$

Table 3 Temperature Dependent Polynomials Material Properties used in the openFoam model obtained from JmatPro[80]

| Property | Polynomial |
|---|---|
| **Liquid** | |
| Density (Kg/m$^3$) | $2.0 * 10^{-8} * T^3 - 2.018 * 10^{-4} * T^2 - 0.3128 * T + 7450$ |
| Specific Heat (J/Kg-K) | 833.08 |
| Thermal Conductivity (W/m-K) | $0.0133 * T + 6.757$ |
| **Solid** | |
| Density (Kg/m$^3$) | $3.0 * 10^{-8} * T^3 - 2.015 * 10^{-4} * T^2 - 0.3736 * T + 7444$ |
| Specific Heat (J/Kg-K) | $2.1 * 10^{-8} * T^3 - 6.706 * 10^{-4} * T^2 + 0.7259 * T + 433.5$ |
| Thermal Conductivity (W/m-K) | $1.0 * 10^{-8} * T^3 - 3.183 * 10^{-5} * T^2 - 0.0270 * T + 16.15$ |

Table 4 Temperature independent properties used in the openFoam model

| Properties | Values |
|---|---|
| Liquidus Temperature (K) | 1620 |
| Solidus Temperature (K) | 1410 |
| Atmosphere Temperature (K) | 300 |
| Preheat Temperature (K) | 443 |
| Convection Coefficient (W/m$^2$-K) | 159 |
| Latent Heat (kJ/kg) | $2.1754 \times 10^{-5}$ |
| Emissivity | 0.4 |

where $Nu_x$ is the Nussel's number, $Re$ is the Reynold's, $Pr$ is the Prandtl's number, and $L$ is the characteristic length and is considered as roughly the length from the gas outflow of the machine to the top surface of the part. Lastly, $k_g$ is the thermal conductivity of the Argon gas. Combining the two equations above results in a relationship that allows for the calculation of the convection coefficient from known dimensions. The combined equation is given as

$$h = \frac{k_g}{L} 0.664 Re_x^{\frac{1}{2}} Pr^{\frac{1}{3}}$$

The resulting parameters for solving the equation to get the convection coefficient are given in Table 4 assuming that $Re = \rho u\, x/\mu$ where $x$ is the length of the part surface in the direction parallel to the gas flow, u is the velocity of the Argon gas flow, $\mu$ is the dynamic viscosity and $\rho$ is the density of the gas.

The geometry used in OpenFOAM replicated the dimensions of the build plate and the first 3mm of a single part geometry. The geometry is presented in Figure 18. Only a single layer was scanned for which it was found that after roughly 15 seconds the scanned part returned to the same temperature as the pre-heat temperature. Therefore, the buildup of heat was not considered to be a concern and the simplification of assuming all layers to follow roughly the same thermal history to be reasonable.

#### *4.1.2 Thermal-Mechanical Model*

The thermal-mechanical simulations were performed in Abaqus. The programming language Python was used to convert the temperature mesh nodal coordinates from OpenFOAM to the Abaqus mesh nodal coordinates. Abaqus subroutines UEXTERNALDB was used to import the nodal temperatures into Abaqus, while UTEMP was used to apply the nodal temperatures at the require coordinates during the simulations. The code for UEXTERNALB and UTEMP subroutines can be found in Appendix A. Each layer had the same thermal profile obtained from the OpenFOAM simulation. This assumption that the thermal profile is roughly the same for all layers was made due to the part in the OpenFOAM simulation reaching preheat temperature before the start of the next layer as mentioned

Table 5 Values used to calculate the convection coefficient

| Properties | Values |
|---|---|
| Prandtl's number | 0.67 [81] |
| Characteristic Length (cm) | 30 |
| Thermal conductivity of gas (W/cm-K) | 0.001791 [81] |
| Density of gas (g/cm$^3$) | 1.61 [81] |
| Dynamic viscosity (g/cm-s) | 0.229x10$^{-3}$ [81] |
| Length of part surface (cm) | 0.05 |

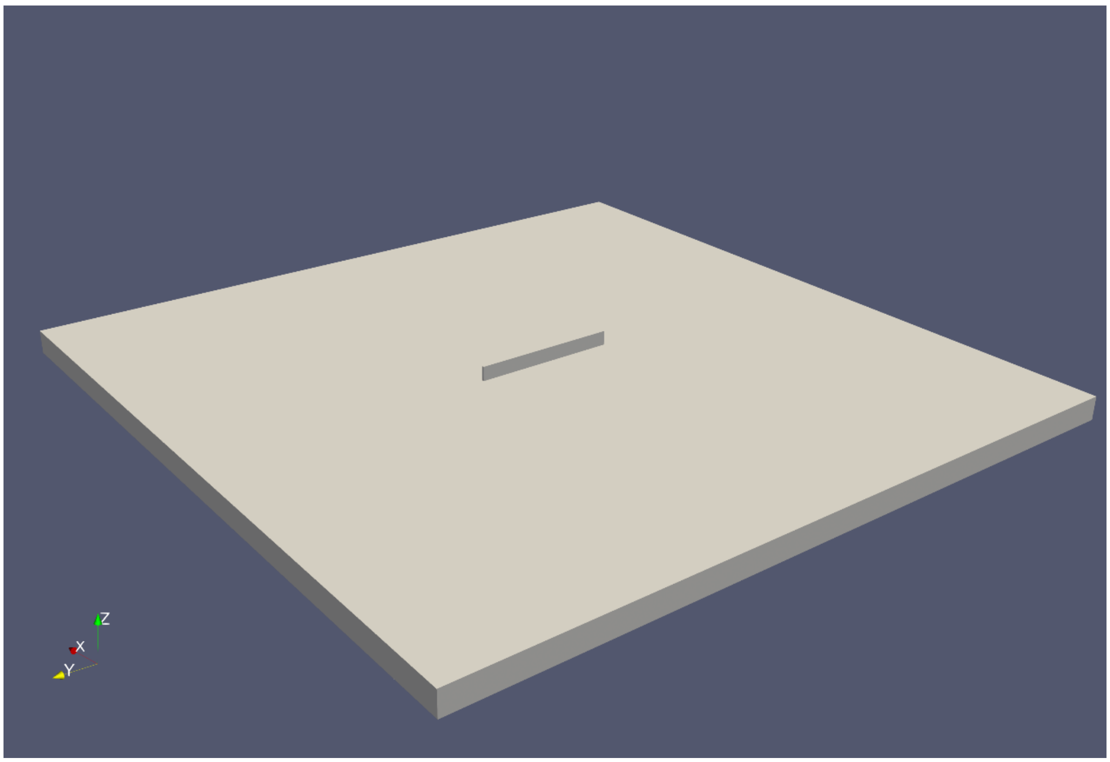


Figure 18 The geometry used in the Open Foam and Abaqus simulations

previously. Therefore, heat buildup within the part was considered to not be a concern. Only a total of 3 layers, each 0.25mm in height, were simulated in the Abaqus simulation due to time constraints and the computational load required to perform the thermal-mechanical simulations with a time accuracy ($\Delta t < 4 * 10^{-5}$s) necessary to capture the scan path. Consolidation of layers will affect the stress values obtained during the simulation, however as this model is qualitative, the expectation is to not obtain exact stress values but instead show trends between different scan patterns. Simulating an actual layer height of 50 μm would be too computationally expensive. The model geometry was the same as the OpenFOAM geometry given in Figure 18. It was chosen to include the build plate in the simulation and have a no displacement boundary condition set for the bottom surface of the build plate for two reasons: 1.) Traditionally during a build, the build plate permits some stressed to be relieved in the part as both the part and build plate are permitted to undergo thermal expansion. Without a build plate a no displacement boundary condition would be placed on the bottom of the part which would result in increases thermal stresses during the scan strategy and residual stresses due to induced limitations on the expansion of material at the boundary condition. Therefore, inclusion of the baseplate results in a more accurate simulation of the residual stresses. 2.) While removal of the build plate may be seen as a way to decrease simulation time by decreasing element count, the resulting increase in stress and resulting increase in plastic deformation results in longer simulation times due to the placement of a no displacement boundary condition on the bottom of the part prevent stress relief through material deformation that would have occurred with the simulation of the base plate. The material data used in the simulation has been attached as a supplementary document and was obtain through JMatPro. Due to difficulty in finding room temperature stress-strain curves for Fe-3Si, the stress-strain curves obtained from JMatPro were calibrated based on high temperature compression test data found in literature [82].

The simulation of stresses within the above model is accomplished using the following governing equation [83]

$$\nabla \cdot \sigma = 0$$

where $\sigma$ is the stress. The relationship between stress and strain is given as [83,84]

$$\sigma_{ij} = C_{ijkl}\varepsilon_{kl} = C\left(\varepsilon_{kl}^{e} + \varepsilon_{kl}^{p} + \varepsilon_{kl}^{t}\right)$$

where $C$ is the fourth-order material stiffness tensor and $\varepsilon_{\mathrm{kl}}^{\mathrm{e}}$, $\varepsilon_{\mathrm{kl}}^{\mathrm{p}}$, and $\varepsilon_{\mathrm{kl}}^{\mathrm{t}}$ are the elastic, plastic, and thermal strain respectively. The thermal strain is given as $\varepsilon_{kl}^{t} = \alpha\delta_{\mathrm{kl}}\Delta T$ [84] where $\alpha$ is the thermal expansion coefficient, $\delta_{kl}$ is the Kronecker delta where $\delta_{kl} = 1$ at $k = l$ and 0 everywhere else, and $\Delta T$ is the temperature change over a given time step. For modelling plasticity, a Von Mises yield criteria was used such that [85]

$$\sigma^0 = \sqrt{\frac{3}{2}S_{ij}S_{ij}}$$

where $S_{ij}$ is the second invariant of the stress deviator and $\sigma_0$ is the yield stress which is obtained through material defined stress strain and temperature curves taken as mentioned previously from JMatPro and calibrated based on high temperature compression test data found in literature [82]. The plastic strain energy is an important criterion for encouraging recrystallization and therefore for determining why the longitudinal scan resulted in grain growth compared to the transverse scan. The elastic strain energy represents internal energy within the sample that results from retained elastic strain in the material and can have an impact on grain growth mechanics. The elastic strain is therefore calculated as [86]

$$E_s = \int_0^t \left( \int_V \sigma_{ij}\dot{\varepsilon}_{ij}^{pl} dV \right) d\tau \tag{1}$$

where $E_s$ is the strain energy, $t$ is time, $\dot{\varepsilon}^{pl}$ is the strain rate, $V$ is the volume of the element, and $\tau$ is an integration variable.

## 4.2 Thermo-Mechanical Simulation Results

The Von Mises stress and the plastic strain results in the XY-plane for the center of the part are given in Figure 19 and Figure 20 respectively for the transverse and longitudinal scan strategies for the third layer at the end of the step at $t = 60$s. Observationally the transverse scan strategy results in a more uniform field of stress compared to the longitudinal scan strategy which shows a greater amount of stress on the right side compared to the left. Overall the variation in max stress and average stress between the two samples is relatively small with an average stress of 1143MPa and 1115MPa and a maximum stress of 1196MPa and 1200MPa for the transverse and longitudinal scan strategies respectively. Looking at the plastic strain results the transverse scan strategy on average saw a higher amount of plastic strain then the longitudinal scan strategy with an average strain of 0.018 and 0.015 for the transverse and longitudinal scan strategy respectively. The fact that the transverse scan strategy sees a higher amount of plastic strain then the longitudinal scan strategy can be explained through the thermal gradients. When thermal gradients are lower, the temperature decrease to the surrounding regions tend to be shallower resulting in more material undergoing greater thermal expansion contributing more to the straining of the material within the surrounding region. Overall the average thermal gradient in the transverse scan strategy is lower therefore it sees greater plastic strains as more regions will see material under thermal expansion. Experimentally, the transverse scan strategy having higher plastic strain is reasonable. During the builds it was noted that samples produced using the transverse scan strategy failed on average around a 19.0mm build height while samples produced using the longitudinal scan strategy failed on average around a 27.3mm build height, likely indicating that the amount of strain that the transverse scan strategy is receiving is higher than the longitudinal scan strategy.

Overall, elastic strain energy is a major driving force for recrystallization and grain growth as it contributes to the stored energy within the system [87,88]. It should be noted however that the elastic strain energy presented in Figure 21 and obtained using equation 1 from section 4.1.2 only accounts for contributions due to the fluctuating thermal stresses experienced by the AM processes resulting in accumulated strain within the samples due to thermal expansion and contraction of material. A second contribution to the elastic strain

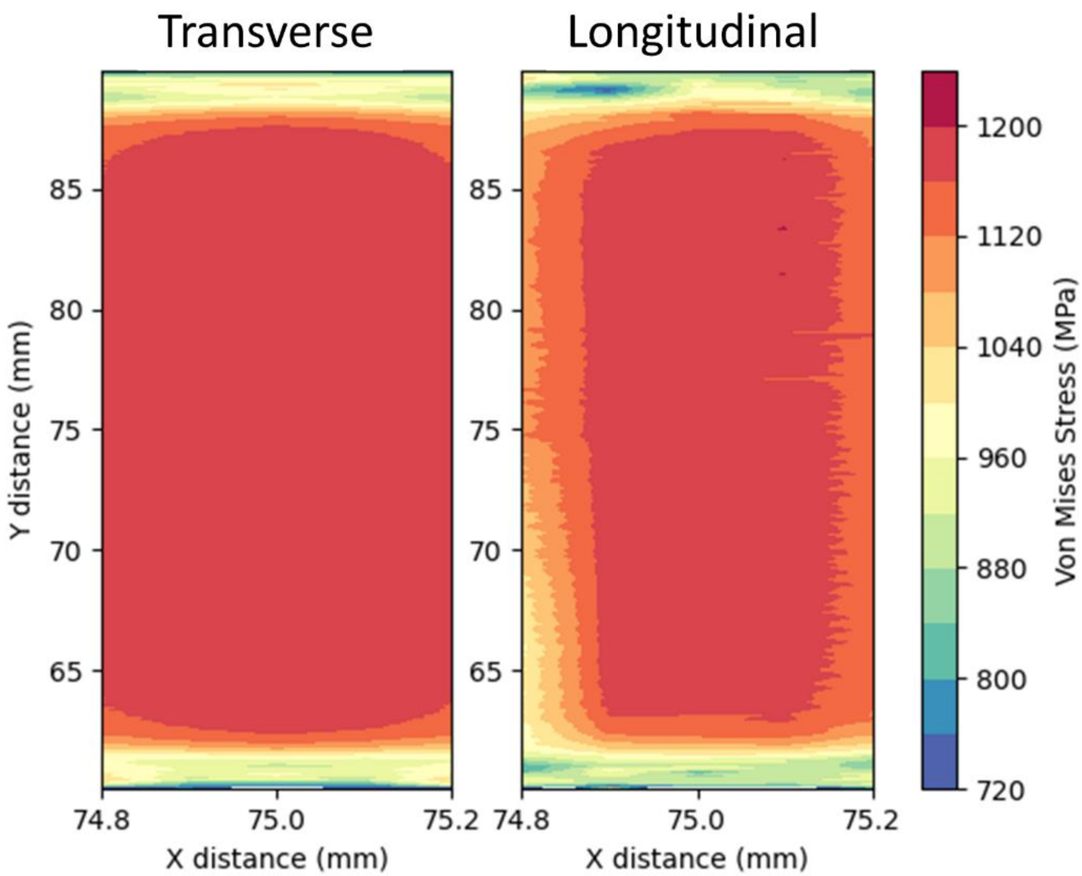


Figure 19 Von mises stress in the XY-plane for the transverse and longitudinal scan strategy at the center of the part after 3 layers

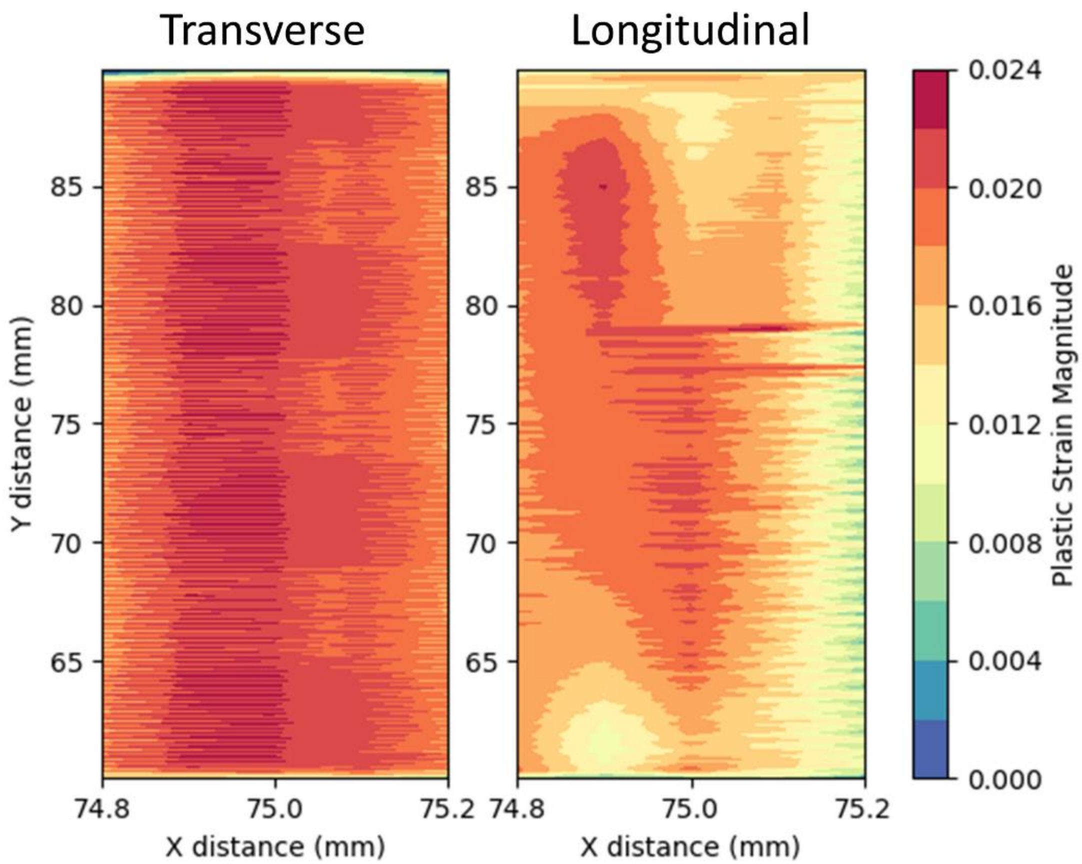


Figure 20 Plastic Strain Magnitude in the XY-plane for the transverse and longitudinal scan strategy at the center of the part after 3 layers

energy and the stored energy in the system is the dislocation density within the samples [87–89]. Dislocations contribute to the elastic strain energy and the store energy within the system by distorting the lattice around them. In general, Dislocation density's ($\rho$) contribution to the stored energy ($E_D$) in the system can be evaluated such that

$$E_D = c_2 \rho G b^2$$

where $c_2$ is a constant of the order of 0.5, $G$ is the shear modulus, and $b$ is the Burgers vector [35]. The dislocation density is usually correlated to the plastic strain were a higher plastic strain leads to a higher dislocation density [90]. Based on Figure 20, the samples produced using the transverse scan strategy should have a larger number of dislocations and therefore a higher amount of stored energy that is not being considered in the elastic strain energy plot in Figure 21.

Further considerations need to be made on the exact method at which grain growth may occur. It has been reported that under cases with high strain and dislocation densities then the nucleation and growth of new grains dominate, but under cases of lower strain then grain boundary migration will be more common [35,89]. With the current EBSD data no assertion can be made if the nucleation and growth of new grains is the primary mechanism influencing the final microstructure in the annealed samples, or if grain boundary migration of certain grain orientations is occurring such that grains with lower strain energies are growing such to minimize the strain energy of the entire system. Currently, due to the multiple potential mechanisms that effect the recrystallization and growth of new grains during annealing it cannot be asserted how the differences in stress and strain within the transverse and longitudinal scan strategies could be having an effect on the annealed microstructure without further characterization.

## 4.3 Thermal Mechanical Model Limitations

It should be noted certain limitations within the thermal-mechanical simulation. The first noted limitation is the assumption that each layer is 250um instead of 50um (i.e. layer consolidation). Due to this limitation the overall stresses seen within the model diverge from the actual stress within the actual samples. Experimental work has however shown

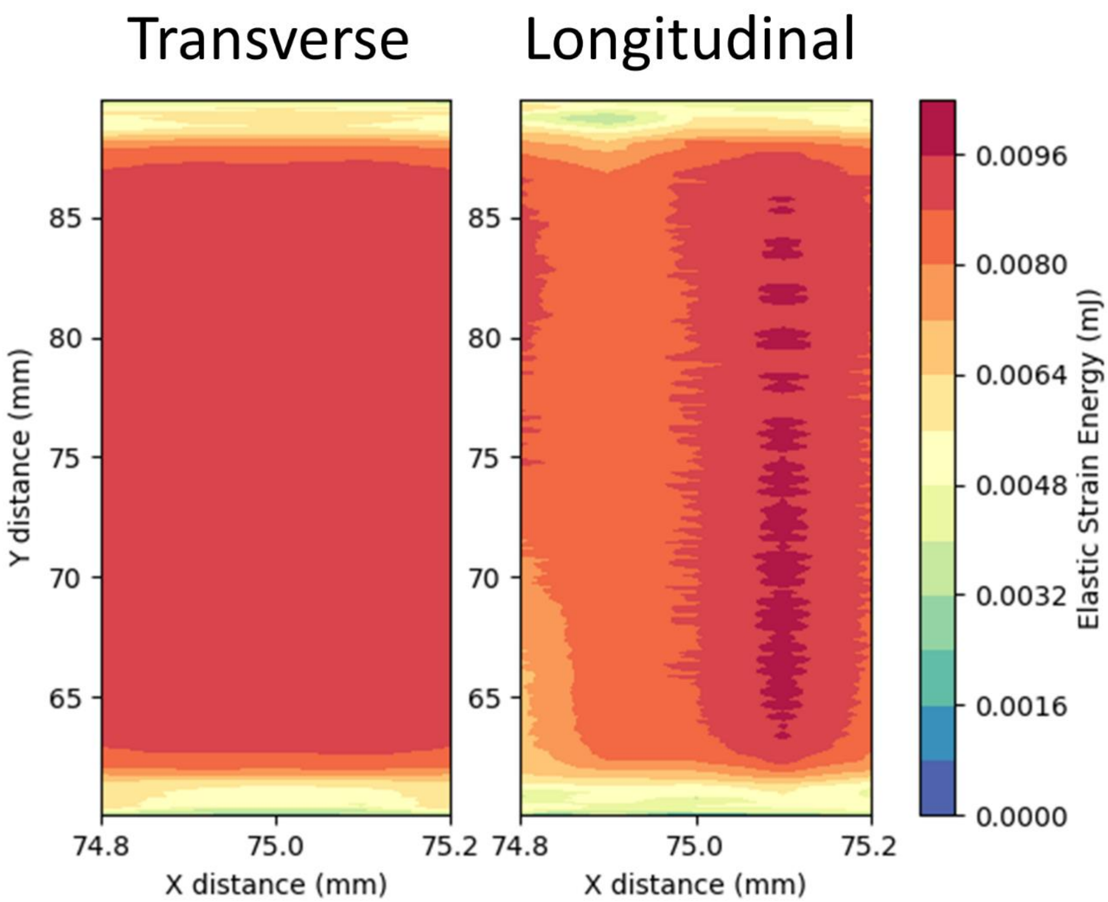


Figure 21 Elastic strain energy in the XY-plane for the transverse and longitudinal scan strategy at the center of the part after 3 layers

that consolidating 4 layers as done here still shows relatively comparable trends in reported stress [91]. Further, as mentioned previously the larger layer heights were done due to computational limitations and was considered acceptable due to only looking for a relative comparison between the two scan strategies and not absolute stress values. A second limitation is noticeable in the artifacting (here seen as horizontal striations) present in Figure 19, Figure 20, and Figure 21. The artifacting appears to repeat about every 250um in the y direction which matches the element count. There is a likelihood that due to the lower resolution of the Abaqus mesh compared to the OpenFOAM mesh there are artifacts occurring. Particularly, looking at the melt pool shape for both the OpenFOAM and Abaqus mesh in Figure 22 for the transverse scan strategy at $t = 0.0319$s it is clear that the resolution of the Abaqus mesh does not allow for the full capture of the melt pool geometry which is likely contributing to the gyrations seen in the reported stress and strain values along the y direction. To fix the artifacting would likely require either decreasing the element size which will further increase computational time or consider the use of a remeshing scheme [49].

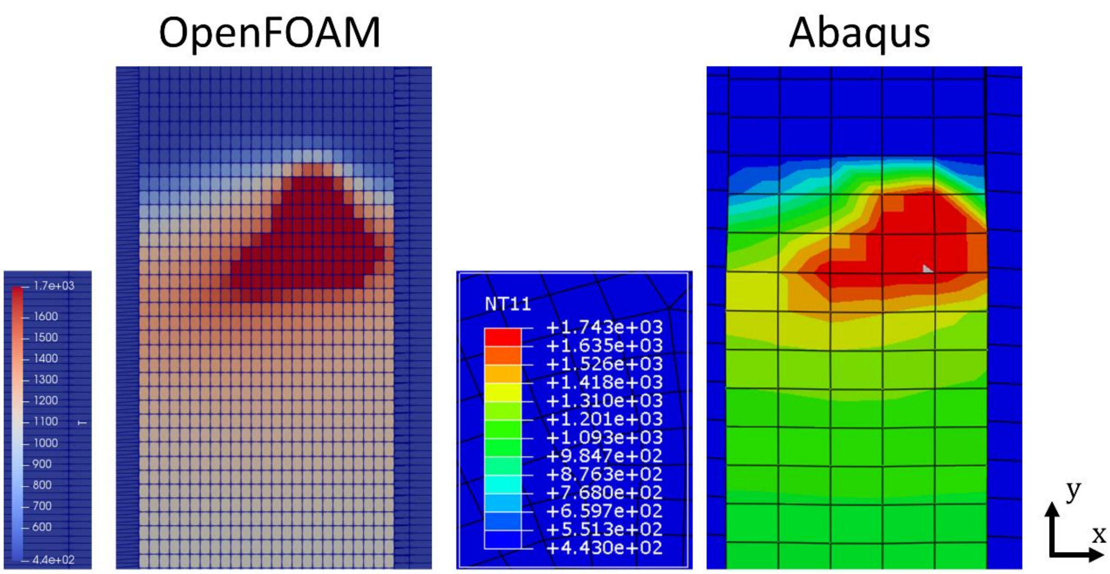


Figure 22 Comparison of the melt pool in OpenFOAM and abaqus at $t = 0.0319$s for the transverse scan strategy.

# CHAPTER 5: RECOMMENDATIONS AND SUMMARY

This work highlights potential causes for the relationship between scan strategy and its resulting influence on the annealed microstructure. Overall it demonstrated how scan strategy can change the as-built microstructure which can subsequently change the resulting annealed microstructure. However, future work still needs to be conducted on developing a full scientific understanding of the effects that different solidification regimes, which are influenced through different processing parameters, influence the annealed Fe-3Si microstructure in AM processes. Particularly, a full understanding of the contributions from grain texture, size, misorientation, boundary pinning and induced plastic strain on the abnormal grain growth within AM needs to be established.

Works under traditional manufacturing techniques have continued to show the influence grain texture, size, and misorientation have on influencing abnormal grain growth for which this work touches on. EBSD serves as a good initial characterization technique to establish the effects that scan strategies have on the annealed microstructure, however the large grain structures in the annealed samples makes it hard to use EBSD to collect a statistical relevant number of grains to assert how as-built grain texture, size and misorientation effect the resulting annealed microstructure . Therefore, characterization techniques such as x-ray or neutron diffraction have to be utilized [22,92]. These techniques would allow for the collection of much larger datasets that would allow for quantitative observations pertaining to the effects of grain texture, size and misorientation, with neutron diffraction being particularly ideal due to the possibility to perform in-situ annealing such that changes within the grains could be captured *in situ* during the annealing process.

A second consideration for future works is the possible effects of grain boundary pinning. The existence of particles is known in traditional manufacturing of Fe-3Si to inhibit grain growth through the pinning of grain boundaries. Under AM oxides present within samples is common due to the large surface area present on powder particles where oxide layers are formed. These oxide layers are usually then deposited into the samples during melting of the powder [93,94]. Further recent work has shown a relationship between energy input and the amount of oxides present in parts produced using L-PBF, showing that higher energy input results in lower number of oxides [95]. Seeing as how the longitudinal scan strategy which has a higher energy input then the transverse scan strategy saw faster abnormal grain growth comparatively, the potential for differences in oxide content within the samples and their effect on grain growth cannot be ruled out. This theory should be relatively easy to confirm through the use of SEM or TEM techniques to locate the presence of oxides within the sample.

Lastly, the results presented here on the residual plastic strain has not been verified only correlated through simulations and observations of resulting microstructure. For validating the analysis on residual plastic strain within AM samples and its effect on the abnormal grain growth both in-situ experiments and measurements of residual stress is possible. Devices such as the Gleeble allow for the in-situ testing of the effects of residual and thermal strain on the grain growth mechanics. The Gleeble would allow for the systematic testing of different strain amounts, and annealing routines. For looking at differences in strain amounts in thin-wall AM samples, techniques such as neutron diffraction and X-ray diffraction have been used to calculate the amount of residual stress [13,50,96,97]. These techniques can be used to verify the results from the thermal-mechanical simulations presented here.

Overall, the main findings of this work can be summarized as followed:

- From the two scan strategies tested (Transverse and Longitudinal) the thermal simulations showed a clear difference in melt pool shape and size. The transverse scan strategy was noted to have a large melt pool that snaked back and forth across the sample while the longitudinal scan strategy was noted to be smaller while presenting a more modulated shape due to the pulse laser on the Renishaw system.
- The as-built EBSD results showed highly textured long epitaxial growth for the transverse scan strategy with grains tilted away from the <100> build direction while the longitudinal scan strategy was noted to have small grain with less overall texture, however a notable number of grains were still oriented within the <100> build direction
- From the as-built EBSD results and thermal gradients calculated from the thermal simulation it was shown that the thermal gradients play a role in influencing the differences in grain structure. Specifically, the direction of the

thermal gradient which influence the dendritic growth direction was correlated to observed differences in grain size and texture where transverse having a more consistent thermal gradient resulted in larger more texture grains compared to the longitudinal scan strategy.

- Within the annealed EBSD builds the transverse scan strategy did not see any abnormal grain growth, however there were striations that had formed throughout the sample that could have been the initial stages of newly nucleated grains. The longitudinal scans however saw large amounts of abnormal grain growth. Grain misorientation and size were both observed as possible reasons for the occurrence of abnormal grain growth in the longitudinal scan strategy and not the transverse scan strategy. No observation however could be made on whether grain orientation played a role in the abnormal grain growth due to the lack in a statically relevant number of grains within the Annealed EBSD
- Results from the thermo-mechanical simulation showed only marginally higher von mises stress in the transverse scan strategy. Plastic strain on the other hand was noted to be noticeable higher in the transverse scan. When it came to strain energy however, the longitudinal scan strategy strain energy was noted to be higher. The higher strain energy was largely attributed to differences in thermal gradients likely resulting in higher strain rates. In relation to abnormal grain growth, both plastic strain through increasing dislocation density and elastic strain energy contribute to the stored energy in the system which influences when and how quickly abnormal grain growth occurs. Therefore no strong conclusions can be made on how differences in plastic and elastic strain between the two scan strategies may be effecting the abnormal grain growth.

# LIST OF REFERENCES

[1] W.J. Sames, F.A. List, S. Pannala, R.R. Dehoff, S.S. Babu, The metallurgy and processing science of metal additive manufacturing, Int. Mater. Rev. 61 (2016) 315–360. doi:10.1080/09506608.2015.1116649.

[2] Y. Zhang, L. Wu, X. Guo, S. Kane, Y. Deng, Y.G. Jung, J.H. Lee, J. Zhang, Additive Manufacturing of Metallic Materials: A Review, J. Mater. Eng. Perform. 27 (2018) 1–13. doi:10.1007/s11665-017-2747-y.

[3] A.T. Polonsky, M.P. Echlin, W.C. Lenthe, R.R. Dehoff, M.M. Kirka, T.M. Pollock, Defects and 3D structural inhomogeneity in electron beam additively manufactured Inconel 718, Mater. Charact. 143 (2018) 171–181. doi:10.1016/j.matchar.2018.02.020.

[4] D.D. Gu, W. Meiners, K. Wissenbach, R. Poprawe, Laser additive manufacturing of metallic components: materials, processes and mechanisms, Int. Mater. Rev. 57 (2012) 133–164. doi:10.1179/1743280411Y.0000000014.

[5] M. Tang, P.C. Pistorius, S. Narra, J.L. Beuth, Rapid Solidification: Selective Laser Melting of AlSi10Mg, Jom. 68 (2016) 960–966. doi:10.1007/s11837-015-1763-3.

[6] S. Li, H. Xiao, K. Liu, W. Xiao, Y. Li, X. Han, J. Mazumder, L. Song, Melt-pool motion, temperature variation and dendritic morphology of Inconel 718 during pulsed- and continuous-wave laser additive manufacturing: A comparative study, Mater. Des. 119 (2017) 351–360. doi:10.1016/j.matdes.2017.01.065.

[7] W.J. Sames, K.A. Unocic, R.R. Dehoff, T. Lolla, S.S. Babu, Thermal effects on microstructural heterogeneity of Inconel 718 materials fabricated by electron beam melting, J. Mater. Res. 29 (2014) 1920–1930. doi:10.1557/jmr.2014.140.

[8] A. Plotkowski, O. Rios, N. Sridharan, Z. Sims, K. Unocic, R.T. Ott, R.R. Dehoff, S.S. Babu, Evaluation of an Al-Ce alloy for laser additive manufacturing, Acta Mater. 126 (2017) 507–519. doi:10.1016/j.actamat.2016.12.065.

[9] A. Plotkowski, J. Pries, F. List, P. Nandwana, B. Stump, K. Carver, R.R. Dehoff, Influence of scan pattern and geometry on the microstructure and soft-magnetic performance of additively manufactured Fe-Si, Addit. Manuf. 29 (2019) 100781. doi:10.1016/j.addma.2019.100781.

[10] L.N. Carter, C. Martin, P.J. Withers, M.M. Attallah, The influence of the laser scan strategy on grain structure and cracking behaviour in SLM powder-bed fabricated nickel superalloy, J. Alloys Compd. 615 (2014) 338–347.

doi:10.1016/j.jallcom.2014.06.172.

[11] M. Haines, A. Plotkowski, C.L. Frederick, E.J. Schwalbach, S.S. Babu, A sensitivity analysis of the columnar-to-equiaxed transition for Ni-based superalloys in electron beam additive manufacturing, Comput. Mater. Sci. 155 (2018) 340–349. doi:10.1016/j.commatsci.2018.08.064.

[12] C.L. Frederick, A. Plotkowski, M.M. Kirka, M. Haines, A. Staub, E.J. Schwalbach, D. Cullen, S.S. Babu, Geometry-Induced Spatial Variation of Microstructure Evolution During Selective Electron Beam Melting of Rene-N5, Metall. Mater. Trans. A Phys. Metall. Mater. Sci. 49 (2018) 5080–5096. doi:10.1007/s11661-018-4793-y.

[13] L.M. Sochalski-Kolbus, E. a. Payzant, P. a. Cornwell, T.R. Watkins, S.S. Babu, R.R. Dehoff, M. Lorenz, O. Ovchinnikova, C. Duty, Comparison of Residual Stresses in Inconel 718 Simple Parts Made by Electron Beam Melting and Direct Laser Metal Sintering, Metall. Mater. Trans. A. (2015). doi:10.1007/s11661-014-2722-2.

[14] P. Prabhakar, W.J. Sames, R. Dehoff, S.S. Babu, Computational modeling of residual stress formation during the electron beam melting process for Inconel 718, Addit. Manuf. 7 (2015) 83–91. doi:10.1016/j.addma.2015.03.003.

[15] R.M. Bozorth, Ferromagnetism, John Wiley & Sons, inc., Hoboken, 2003.

[16] M.F. Littmann, Iron and Silicon-Iron Alloys, IEEE Trans. Magn. 7 (1971) 48–60. doi:10.1109/TMAG.1971.1066998.

[17] J.N. Lemke, M. Simonelli, M. Garibaldi, I. Ashcroft, R. Hague, M. Vedani, R. Wildman, C. Tuck, Calorimetric study and microstructure analysis of the order-disorder phase transformation in silicon steel built by SLM, J. Alloys Compd. 722 (2017) 293–301. doi:10.1016/j.jallcom.2017.06.085.

[18] D. Goll, D. Schuller, G. Martinek, T. Kunert, J. Schurr, C. Sinz, T. Schubert, T. Bernthaler, H. Riegel, G. Schneider, Additive manufacturing of soft magnetic materials and components, Addit. Manuf. 27 (2019) 428–439. doi:10.1016/j.addma.2019.02.021.

[19] M. Garibaldi, I. Ashcroft, M. Simonelli, R. Hague, Metallurgy of high-silicon steel parts produced using Selective Laser Melting, Acta Mater. 110 (2016) 207–216. doi:10.1016/j.actamat.2016.03.037.

[20] M. Garibaldi, I. Ashcroft, N. Hillier, S.A.C. Harmon, R. Hague, Relationship between laser energy input, microstructures and magnetic properties of selective laser melted

Fe-6.9%wt Si soft magnets, Mater. Charact. 143 (2018) 144–151. doi:10.1016/j.matchar.2018.01.016.

[21] M. Garibaldi, I. Ashcroft, J.N. Lemke, M. Simonelli, R. Hague, Effect of annealing on the microstructure and magnetic properties of soft magnetic Fe-Si produced via laser additive manufacturing, Scr. Mater. 142 (2018) 121–125. doi:10.1016/j.scriptamat.2017.08.042.

[22] S. Birosca, A. Nadoum, D. Hawezy, F. Robinson, W. Kockelmann, Mechanistic approach of Goss abnormal grain growth in electrical steel: Theory and argument, Acta Mater. 185 (2020) 370–381. doi:10.1016/j.actamat.2019.12.023.

[23] S. Mishra, C. Därmann, K. Lücke, On the development of the goss texture in iron-3% silicon, Acta Metall. 32 (1984) 2185–2201. doi:10.1016/0001-6160(84)90161-5.

[24] A. Morawiec, On abnormal growth of Goss grains in grain-oriented silicon steel, Scr. Mater. 64 (2011) 466–469. doi:10.1016/j.scriptamat.2010.11.013.

[25] F. Fang, Y. Zhang, X. Lu, Y. Wang, G. Cao, G. Yuan, Y. Xu, G. Wang, R.D.K. Misra, Inhibitor induced secondary recrystallization in thin-gauge grain oriented silicon steel with high permeability, Mater. Des. 105 (2016) 398–403. doi:10.1016/j.matdes.2016.05.091.

[26] M. Baricco, E. Mastrandrea, C. Antonione, B. Viala, T. Degauque, E. Ferrara, F. Fiorillo, Grain growth and texture in rapidly solidified Fe(S) 6.5 wt.% ribbons, Mater. Sci. Eng. 228 (1997) 1025–1029.

[27] D. Dorner, S. Zaefferer, D. Raabe, Retention of the Goss orientation between microbands during cold rolling of an Fe3 % Si single crystal, Acta Mater. 55 (2007) 2519–2530. doi:10.1016/j.actamat.2006.11.048.

[28] D. Dorner, S. Zaefferer, L. Lahn, D. Raabe, Overview of Microstructure and Microtexture Development in Grain-oriented Silicon Steel, J. Magn. Magn. Mater. 304 (2006) 183–186. doi:10.1016/j.jmmm.2006.02.116.

[29] R. Shimizu, J. Harase, Coincidence grain boundary and texture evolution in Fe-3%Si, Acta Metall. 37 (1989) 1241–1249. doi:10.1016/0001-6160(89)90118-1.

[30] Y. Hayakawa, J.A. Szpunar, A new model of Goss texture development during secondary recrystallization of electrical steel, Acta Mater. 45 (1997) 4713–4720. doi:10.1016/S1359-6454(97)00111-0.

[31] A.A. Redikul'tsev, M.L. Lobanov, G.M. Rusakov, L. V. Lobanova, Secondary recrystallization in Fe-3% Si alloy with (110)[001] single-component texture, Phys. Met. Metallogr. 114 (2013) 33–40. doi:10.1134/S0031918X13010110.

[32] S.F. Castro, J. Gallego, F.J.G. Landgraf, H.J. Kestenbach, Orientation dependence of stored energy of cold work in semi-processed electrical steels after temper rolling, Mater. Sci. Eng. A. 427 (2006) 301–305. doi:10.1016/j.msea.2006.04.092.

[33] N.J. Park, E.J. Lee, H.D. Joo, J.T. Park, Evolution of goss orientation during rapid heating for primary recrystallization in grain-oriented electrical steel, ISIJ Int. 51 (2011) 975–981. doi:10.2355/isijinternational.51.975.

[34] M. Matsuo, T. Sakai, Y. Suga, Origin and Development of Through-the-Thickness Variations of Texture in the Processing of Grain-Oriented Silicon Steel, Metall. Trans. A. 17A (1986) 1313–1322.

[35] F.J. Humphreys, M. Hatherly, Recrystallization and Related Annealing Phenomena, First, Elsevier Science Inc., Tarrytown, 1995.

[36] D.A. Porter, K.E. Easterling, M.Y. Sherif, Phase Transformations in Metals and Alloys, Third, CRC Press, Boca Raton, 2009.

[37] A. 52900:2015, "ISO/ASTM 52900:2015", Standard Terminology for Additive Manufacturing – General Principles – Terminology, ASTM Int. i (2015) 1–9. doi:10.1520/F2792-12A.2.

[38] S.S. Babu, N. Raghavan, J. Raplee, S.J. Foster, C. Frederick, M. Haines, R. Dinwiddie, M.K. Kirka, A. Plotkowski, Y. Lee, R.R. Dehoff, Additive Manufacturing of Nickel Superalloys: Opportunities for Innovation and Challenges Related to Qualification, Metall. Mater. Trans. A Phys. Metall. Mater. Sci. 49 (2018) 3764–3780. doi:10.1007/s11661-018-4702-4.

[39] P.S. Wei, Thermal Science of Weld Bead Defects: A Review, J. Heat Transfer. 133 (2011) 031005. doi:10.1115/1.4002445.

[40] J.P. Kruth, L. Froyen, J. Van Vaerenbergh, P. Mercelis, M. Rombouts, B. Lauwers, Selective laser melting of iron-based powder, J. Mater. Process. Technol. 149 (2004) 616–622. doi:10.1016/j.jmatprotec.2003.11.051.

[41] S. Yoder, P. Nandwana, V. Paquit, M. Kirka, A. Scopel, R.R. Dehoff, S.S. Babu, Approach to qualification using E-PBF in-situ process monitoring in Ti-6Al-4V, Addit. Manuf. 28

(2019) 98–106. doi:10.1016/j.addma.2019.03.021.

[42] L. Thijs, F. Verhaeghe, T. Craeghs, J. Van Humbeeck, J.P. Kruth, A study of the microstructural evolution during selective laser melting of Ti-6Al-4V, Acta Mater. 58 (2010) 3303–3312. doi:10.1016/j.actamat.2010.02.004.

[43] L. Thijs, K. Kempen, J.P. Kruth, J. Van Humbeeck, Fine-structured aluminium products with controllable texture by selective laser melting of pre-alloyed AlSi10Mg powder, Acta Mater. 61 (2013) 1809–1819. doi:10.1016/j.actamat.2012.11.052.

[44] R.R. Dehoff, M.M. Kirka, W.J. Sames, H. Bilheux, A.S. Tremsin, L.E. Lowe, S.S. Babu, Site specific control of crystallographic grain orientation through electron beam additive manufacturing, Mater. Sci. Technol. 31 (2015) 931–938. doi:10.1179/1743284714Y.0000000734.

[45] J. Raplee, A. Plotkowski, M.M. Kirka, R. Dinwiddie, A. Okello, R.R. Dehoff, S.S. Babu, Thermographic Microstructure Monitoring in Electron Beam Additive Manufacturing, Sci. Rep. 7 (2017) 1–16. doi:10.1038/srep43554.

[46] S. Catchpole-Smith, N. Aboulkhair, L. Parry, C. Tuck, I.A. Ashcroft, A. Clare, Fractal scan strategies for selective laser melting of 'unweldable' nickel superalloys, Addit. Manuf. 15 (2017) 113–122. doi:10.1016/j.addma.2017.02.002.

[47] Y.S. Lee, M.M. Kirka, S. Kim, N. Sridharan, A. Okello, R.R. Dehoff, S.S. Babu, Asymmetric Cracking in Mar-M247 Alloy Builds During Electron Beam Powder Bed Fusion Additive Manufacturing, Metall. Mater. Trans. A Phys. Metall. Mater. Sci. 49 (2018) 5065–5079. doi:10.1007/s11661-018-4788-8.

[48] H. Ali, H. Ghadbeigi, K. Mumtaz, Effect of scanning strategies on residual stress and mechanical properties of Selective Laser Melted Ti6Al4V, Mater. Sci. Eng. A. 712 (2018) 175–187. doi:10.1016/j.msea.2017.11.103.

[49] B. Cheng, S. Shrestha, K. Chou, Stress and deformation evaluations of scanning strategy effect in selective laser melting, Addit. Manuf. 12 (2016) 240–251. doi:10.1016/j.addma.2016.05.007.

[50] M.F. Zaeh, G. Branner, Investigations on residual stresses and deformations in selective laser melting, Prod. Eng. 4 (2010) 35–45. doi:10.1007/s11740-009-0192-y.

[51] J.H. Martin, B.D. Yahata, J.M. Hundley, J.A. Mayer, T.A. Schaedler, T.M. Pollock, 3D printing of high-strength aluminium alloys, Nature. 549 (2017) 365–369.

doi:10.1038/nature23894.

[52] S. a. David, J.M. Vitek, Correlation between solidification parameters and weld microstructures, Int. Mater. Rev. 34 (1989) 213–245. doi:10.1179/imr.1989.34.1.213.

[53] J.A. Dantzig, M. Rappaz, Solidification, CRC Press, Boca Raton, Fl., 2009.

[54] N. Raghavan, S. Simunovic, R.R. Dehoff, A. Plotkowski, J. Turner, M.M. Kirka, S.S. Babu, Localized Melt-Scan Strategy for Site Specific Control of Grain Size and Primary Dendrite Arm Spacing in Electron Beam Additive Manufacturing Localized Melt-Scan Strategy for Site Specific Control of Grain Size and Primary Dendrite Arm Spacing in Electron, Acta Mater. 140 (2017) 375–387. doi:10.1016/j.actamat.2017.08.038.

[55] A. Plotkowski, M.M. Kirka, S.S. Babu, Verification and validation of a rapid heat transfer calculation methodology for transient melt pool solidification conditions in powder bed metal additive manufacturing, Addit. Manuf. 18 (2017) 256–268. doi:10.1016/j.addma.2017.10.017.

[56] A. Plotkowski, Geometry-Dependent Solidification Regimes in Metal Additive Manufacturing, Weld. J. 99 (2020) 59S-66S. doi:10.29391/2020.99.006.

[57] M. Gäumann, R. Trivedi, W. Kurz, Nucleation ahead of the advancing interface in directional solidification, Mater. Sci. Eng. A226. 228 (1997) 763–769. doi:10.1016/S0921-5093(97)80081-0.

[58] J. Lipton, W. Kurz, R. Trivedi, Rapid dendrite growth in undercooled alloys, Acta Metall. 35 (1987) 957–964. doi:10.1016/0001-6160(87)90174-X.

[59] R. Trivedi, W. Kurz, Dendritic growth, Int. Mater. Rev. 39 (1994) 49–74.

[60] D.M. Herlach, Non-equilibrium solidification of undercooled metallic metls, Mater. Sci. Eng. R. 12 (2014) 177–272. doi:10.1016/0927-796X(94)90011-6.

[61] M. Gäumann, C. Bezençon, P. Canalis, W. Kurz, Single-crystal laser deposition of superalloys: processing–microstructure maps, Acta Mater. 49 (2001) 1051–1062. doi:10.1016/S1359-6454(00)00367-0.

[62] J.D. Hunt, Steady state columnar and equiaxed growth of dendrites and eutectic, Mater. Sci. Eng. 65 (1984) 75–83. doi:10.1016/0025-5416(84)90201-5.

[63] J.C. Villafuerte, E. Pardo, H.W. Kerr, The effect of alloy composition and welding conditions on columnar-equiaxed transitions in ferritic stainless steel gas-tungsten

arc welds, Metall. Trans. A. 21 (1990) 2009–2019. doi:10.1007/BF02647249.

[64] M. Gäumann, C. Bezençon, P. Canalis, W. Kurz, Single-crystal laser deposition of superalloys: Processing-microstructure maps, Acta Mater. 49 (2001) 1051–1062. doi:10.1016/S1359-6454(00)00367-0.

[65] E.J. Schwalbach, S.P. Donegan, M.G. Chapman, K.J. Chaput, M.A. Groeber, A discrete source model of powder bed fusion additive manufacturing thermal history, Addit. Manuf. 25 (2019) 485–498. doi:10.1016/j.addma.2018.12.004.

[66] P. Bajaj, J. Wright, I. Todd, E.A. Jägle, Predictive process parameter selection for Selective Laser Melting Manufacturing: Applications to high thermal conductivity alloys, Addit. Manuf. 27 (2019) 246–258. doi:10.1016/j.addma.2018.12.003.

[67] P. Mercelis, J.P. Kruth, Residual stresses in selective laser sintering and selective laser melting, Rapid Prototyp. J. 12 (2006) 254–265. doi:10.1108/13552540610707013.

[68] Y.S. Lee, W. Zhang, Modeling of heat transfer, fluid flow and solidification microstructure of nickel-base superalloy fabricated by laser powder bed fusion, Addit. Manuf. 12 (2016) 178–188. doi:10.1016/j.addma.2016.05.003.

[69] S.A. Khairallah, A.T. Anderson, A. Rubenchik, W.E. King, Laser powder-bed fusion additive manufacturing: Physics of complex melt flow and formation mechanisms of pores, spatter, and denudation zones, Acta Mater. 108 (2016) 36–45. doi:10.1016/j.actamat.2016.02.014.

[70] M. Markl, A. Bauereiß, A. Rai, C. Körner, Numerical Investigations of Selective Electron Beam Melting on the Powder Scale, (2016) 1–6.

[71] S. Ly, A.M. Rubenchik, S.A. Khairallah, G. Guss, M.J. Matthews, Metal vapor micro-jet controls material redistribution in laser powder bed fusion additive manufacturing, Sci. Rep. 7 (2017) 1–12. doi:10.1038/s41598-017-04237-z.

[72] C.A. Biffi, J. Fiocchi, P. Bassani, A. Tuissi, Continuous wave vs pulsed wave laser emission in selective laser melting of AlSi10Mg parts with industrial optimized process parameters: Microstructure and mechanical behaviour, Addit. Manuf. 24 (2018) 639–646. doi:10.1016/j.addma.2018.10.021.

[73] E. Assuncao, S. Williams, Comparison of continuous wave and pulsed wave laser welding effects, Opt. Lasers Eng. 51 (2013) 674–680. doi:10.1016/j.optlaseng.2013.01.007.

[74] X. Ding, L. Wang, S. Wang, Comparison study of numerical analysis for heat transfer and fluid flow under two different laser scan pattern during selective laser melting, Optik (Stuttg). 127 (2016) 10898–10907. doi:10.1016/j.ijleo.2016.08.123.

[75] M. Pakniat, F.M. Ghaini, M.J. Torkamany, Hot cracking in laser welding of Hastelloy X with pulsed Nd: YAG and continuous wave fiber lasers, Mater. Des. 106 (2016) 177–183. doi:10.1016/j.matdes.2016.05.124.

[76] J. Coleman, A. Plotkowski, B. Stump, N. Raghavan, A. Sabau, M. Krane, J. Heigel, D.R. Ricker, L. Levine, S. Babu, Sensitivity of Thermal Predictions to Uncertain Surface Tension Data in Laser Additive Manufacturing, J. Heat Transfer. (2020). doi:10.1115/1.4047916.

[77] C. Körner, H. Helmer, A. Bauereiß, R.F. Singer, Tailoring the grain structure of IN718 during selective electron beam melting, MATEC Web Conf. 14 (2014) 08001. doi:10.1051/matecconf/20141408001.

[78] N. Raghavan, S. Simunovic, R. Dehoff, A. Plotkowski, J. Turner, M. Kirka, S. Babu, Localized melt-scan strategy for site specific control of grain size and primary dendrite arm spacing in electron beam additive manufacturing, Acta Mater. 140 (2017) 375–387. doi:10.1016/j.actamat.2017.08.038.

[79] J. Goldak, A. Chakravarti, M. Bibby, A new finite element model for welding heat sources, Metall. Trans. B. 15 (1984) 299–305. doi:10.1007/BF02667333.

[80] JmatPro Ver. 9, (n.d.).

[81] A. Jaques, Thermophysical properties of argon, Batavia, IL, 1988. doi:10.2172/5025437.

[82] J.-P.A. Immarigeon, J.J. Jonas, The Deformation of Armco Iron and Silicon Steel in the Vicinity of the Curie Temperature, Acta Metall. 22 (1974) 1235–1247.

[83] C. Li, J.F. Liu, X.Y. Fang, Y.B. Guo, Efficient predictive model of part distortion and residual stress in selective laser melting, Addit. Manuf. 17 (2017) 157–168. doi:10.1016/j.addma.2017.08.014.

[84] T. Mukherjee, W. Zhang, T. DebRoy, An improved prediction of residual stresses and distortion in additive manufacturing, Comput. Mater. Sci. 126 (2017) 360–372. doi:10.1016/j.commatsci.2016.10.003.

[85] Abaqus Documentation version 2017, (2017).

[86] Abaqus Documentation version 2017, (2017).

[87] K. Chen, R. Huang, Y. Li, S. Lin, W. Zhu, N. Tamura, J. Li, Z.W. Shan, E. Ma, Rafting-Enabled Recovery Avoids Recrystallization in 3D-Printing-Repaired Single-Crystal Superalloys, Adv. Mater. 32 (2020) 1–8. doi:10.1002/adma.201907164.

[88] D.N. Lee, H.T. Jeong, H.J. Shin, The evolution of recrystallization textures in plastically deformed face centered cubic metals, Met. Mater. Int. 4 (1998) 391–396. doi:10.1007/BF03187798.

[89] H.R. Wenk, G. Canova, Y. Bréchet, L. Flandin, A deformation-based model for recrystallization of anisotropic materials, Acta Mater. 45 (1997) 3283–3296. doi:10.1016/S1359-6454(96)00409-0.

[90] G.E. Dieter, Mechanical Metallurgy, First, McGraw-Hill Book Company, New York, 1961.

[91] A. Kiran, J. Hodek, J. Vavřík, M. Urbánek, J. Džugan, Numerical Simulation Development and Computational Optimization for Directed Energy Deposition Additive Manufacturing Process, Materials (Basel). 13 (2020) 2666. doi:10.3390/ma13112666.

[92] M. Frommert, C. Zobrist, L. Lahn, A. Böttcher, D. Raabe, S. Zaefferer, Texture measurement of grain-oriented electrical steels after secondary recrystallization, J. Magn. Magn. Mater. 320 (2008) 657–660. doi:10.1016/j.jmmm.2008.04.102.

[93] D. Galicki, F. List, S.S. Babu, A. Plotkowski, H.M. Meyer, R. Seals, C. Hayes, Localized Changes of Stainless Steel Powder Characteristics During Selective Laser Melting Additive Manufacturing, Metall. Mater. Trans. A. (2019). doi:10.1007/s11661-018-5072-7.

[94] F. Yan, W. Xiong, E. Faierson, G.B. Olson, Characterization of nano-scale oxides in austenitic stainless steel processed by powder bed fusion, Scr. Mater. 155 (2018) 104–108. doi:10.1016/j.scriptamat.2018.06.011.

[95] M.P. Haines, N.J. Peter, S.S. Babu, E.A. Jägle, In-situ synthesis of oxides by reactive process atmospheres during L-PBF of stainless steel, Addit. Manuf. 33 (2020). doi:10.1016/j.addma.2020.101178.

[96] E. Cakmak, M.M. Kirka, T.R. Watkins, R.C. Cooper, K. An, H. Choo, W. Wu, R.R. Dehoff, S.S. Babu, Microstructural and micromechanical characterization of IN718 theta

shaped specimens built with electron beam melting, Acta Mater. 108 (2016) 161–175. doi:10.1016/j.actamat.2016.02.005.

[97] I. Yadroitsev, I. Yadroitsava, Evaluation of residual stress in stainless steel 316L and Ti6Al4V samples produced by selective laser melting, Virtual Phys. Prototyp. 10 (2015) 67–76. doi:10.1080/17452759.2015.1026045.

# APPENDIX

## A. Abaqus Subroutines

```
!DIR$ FREEFORM
SUBROUTINE UEXTERNALDB(LOP,LRESTART,TIME,DTIME,KSTEP,KINC)

    INCLUDE 'ABA_PARAM.INC'

    DIMENSION TIME(2)

    DIMENSION INTV(4),REALV(4)
    CHARACTER*8 CHARV(4)

    INTEGER FILEHANDLE, NODE, LAYER
    CHARACTER*75 FILENAME
    REAL z_coords, x, y, z
    INTEGER, PARAMETER :: TIME_LENGTH = 12856
    INTEGER, PARAMETER :: NODE_LENGTH = 7224

    REAL time_data(TIME_LENGTH), T(TIME_LENGTH, NODE_LENGTH), x_coords,
y_coords,  nodes(NODE_LENGTH)
    COMMON /SIMDATA/ time_data, T, x_coords, y_coords, nodes

    IF (LOP == 0) THEN
        FILEHANDLE = 102

        !    Read the number of points
        IF (KSTEP == 0) THEN
            DO I=1,TIME_LENGTH
                WRITE (FILENAME, fmt='(a,i0)') 'E:\0_scan\T\T_', I

                OPEN (UNIT=FILEHANDLE, FILE=FILENAME, STATUS='OLD')
                READ(FILEHANDLE, *) time_data(I+1)
                ! REALV(1) = time_data(I+1)
                ! CALL STDB_ABQERR(1,'%R',INTV,REALV,CHARV)
                DO J=1,NODE_LENGTH
                    READ(FILEHANDLE, *) T(I+1,J), x_coords, y_coords,
z_coords
                    ! REALV(1) = J
                    ! REALV(2) = x_coords(J)
                    ! CALL STDB_ABQERR(1,'%R, %R',INTV,REALV,CHARV)
                END DO
                CLOSE(FILEHANDLE)
            END DO
        END IF

        ! REALV(1) = time_data(4000)
        ! CALL STDB_ABQERR(1,'%R',INTV,REALV,CHARV)

    ELSE IF (LOP == 5) THEN

        REALV(1) = mod(KSTEP, 2)
        REALV(2) = (KSTEP+1)/2 - 1
```

```
        CALL STDB_ABQERR(1,'%R %R',INTV,REALV,CHARV)


        LAYER = KSTEP - 1
        WRITE (FILENAME, fmt='(a,i0)') 'E:\0_scan\NN\NNL_', LAYER
        OPEN  (FILEHANDLE, FILE=FILENAME, STATUS='OLD')

        READ(FILEHANDLE, *)

        IF (LAYER == 0) THEN
             DO I=1,1806
                READ(FILEHANDLE, *) nodes(I), x, y, z
            END DO
        ELSE IF (LAYER==1) THEN
            DO I=1,3612
                READ(FILEHANDLE, *) nodes(I), x, y, z
            END DO
        ELSE IF (LAYER==2) THEN
            DO I=1,5418
                READ(FILEHANDLE, *) nodes(I), x, y, z
            END DO
        ELSE
            DO I=1,7224
                READ(FILEHANDLE, *) nodes(I), x, y, z
            END DO
        END IF

        CLOSE(FILEHANDLE)

    END IF

    RETURN
END

SUBROUTINE UTEMP(TEMP,NSECPT,KSTEP,KINC,TIME,NODE,COORDS)
    INCLUDE 'ABA_PARAM.INC'

    DIMENSION TEMP(NSECPT), TIME(2), COORDS(3)

    DIMENSION INTV(4),REALV(13)
    CHARACTER*8 CHARV(4)

    REAL NODE_INDEX
    INTEGER, PARAMETER :: TIME_LENGTH = 12856
    INTEGER, PARAMETER :: NODE_LENGTH = 7224

    REAL time_data(TIME_LENGTH), T(TIME_LENGTH, NODE_LENGTH), x_coords,
y_coords,  nodes(NODE_LENGTH)
    COMMON /SIMDATA/ time_data, T, x_coords, y_coords, nodes

    NODE_INDEX = -1

    TEMP(1) = 443
```

```
    IF (TIME(1) > time_data(TIME_LENGTH)) THEN
        TEMP(1) = 443
        GOTO 999
    END IF

    IF (ANY(nodes .EQ. NODE)) THEN
        ILOOP: DO I=1,SIZE(nodes)
            IF (NODE==nodes(I)) THEN
                NODE_INDEX = I
                EXIT ILOOP
            END IF
        END DO ILOOP
    END IF
    IF (NODE_INDEX .NE. -1) THEN
        JLOOP: DO I=2,SIZE(time_data)
            IF (TIME(1) .LE. time_data(I)) THEN
                TEMP(1) = T(I, NODE_INDEX) + (T(I-1, NODE_INDEX) - T(I,
NODE_INDEX)) * (TIME(1) - time_data(I)) / (time_data(I-1) -
time_data(I))
                EXIT JLOOP
            END IF
        END DO JLOOP

        IF (TEMP(1) .LT. 443) THEN
            TEMP(1) = 443
        ELSE IF (TEMP(1) .GT. 1743) THEN
            TEMP(1) = 1743
        END IF
    END IF

999 RETURN
END
```

# VITA

Michael Haines was born in Knoxville, TN and graduated from Farragut High School in 2014. During his time at Farragut High School he would be an active participant in FIRST robotic, which would influence his decision to pursue research into Additive Manufacturing (AM). He would then go on to the University of Tennessee to pursue a bachelor's degree in Mechanical Engineering where he spent three years as an undergraduate research assistant working with the additive manufacturing of nickel alloys under the electron powder bed fusion process. He would get his degree from the University of Tennessee in 2017. He then spent six months in Germany as a guest researcher at the Max Planck Institut Für Eisenforschung researching the production of oxide dispersion alloys in AM. Afterwards, he returned to UT to complete his master's degree in mechanical engineering continuing his focus on AM research. Since starting his research in AM, Michael has published two papers and looks to continues to contribute to the research in AM and next plans to pursue his PhD.